arXiv:astro-ph/0411298v1 11 Nov 2004

Integral Field Spectroscopy of the central regions of 3C 120: Evidence of a past merging event

B.Garcia-Lorenzo[1], S.F Sánchez[2], E.Mediavilla[1], J.I. González-Serrano[3,4], L.Christensen[2]

bgarcia@ll.iac.es

ABSTRACT

Optical integral field spectroscopy (IFS) combined with Hubble Space Telescope (HST) WFPC imaging were used to characterize the central regions of the Seyfert 1 radio galaxy 3C 120. We carried out the analysis of the data, deriving intensity maps of different emission lines and the continua at different wavelengths from the observed spectra. Applying a 2D modeling to the HST images we decoupled the nucleus and the host galaxy, and analyzed the host morphology. The host is a highly distorted bulge dominated galaxy, rich in substructures. We developed a new technique to model the IFS data extending the 2D modeling (3D modeling hereafter). Using this technique we separated the Seyfert nucleus and the host galaxy spectra, and derived a residual data cube with spectral and spatial information of the different structures in 3C 120. Three continuum-dominated structures (named A, B, and C) and other three extended emission line regions (EELRs, named E_1, E_2 and E_3) are found in 3C 120 which does not follow the general behavior of a bulge dominated galaxy. We also found shells in the central kpc that may be remnants of a past merging event in this galaxy. The origin of E_1 is most probably due to the interaction of the radio-jet of 3C 120 with the intergalactic medium (Axon et al. 1989; Sánchez et al. 2004a). Structures A, B, and the shell at the southeast of the nucleus seem to correspond to a larger morphological clumpy structure that may be a tidal tail, consequence of the past merging event. We found a bright EELR (E_2) in the innermost part of this tidal tail, nearby the nucleus, which shows a high ionization level. The kinematics of the E_2 region and its connection to the tidal tail suggest that the tail has channeled gas from the outer regions to the center.

[1]Instituto de Astrofísica de Canarias, 38205 La Laguna, Tenerife, Spain

[2]Astrophysikalisches Institut Potsdam, An der Sternwarte 16, 14482 Potsdam, Germany

[3]Instituto de Fisica de Cantabria, UC-CSIC, Av. de Los Castros S/N, 35005, Santander, Spain

[4]Dept. de Fisica Moderna, Facultad de Ciencias, UC, Av. de Los Castros S/N, 35005, Santander, Spain

Subject headings: galaxies: individual: 3C 120 — galaxies: ionized gas and stellar kinematics and dynamics — galaxies: Seyfert

1. Introduction

Radio galaxies are excellent laboratories to disentangle the role of central active nuclei in host galaxies evolution and the relation of intergalactic environment and the central activity. The complex structure of radio galaxies put severe troubles to carry out specific optical studies in this matter. Fortunately, the recent technical and computational improvements on integral field spectroscopy (IFS hereafter) open new frontiers to multitude of astronomical projects. In the particular case of radio galaxies, IFS data allow to separate the different components and to perform an independent analysis of the various subsystems and their evolution.

3C 120 is a Seyfert 1 galaxy at a redshift of $z = 0.033$. It has been studied extensively at many wide-range wavelengths, with special attention in X-ray and radio frequencies (e.g. Walker et al. 1987; Moles et al. 1988; Walker 1997; Ogle et al. 2004). Although 3C 120 was classified as an early-type galaxy based on a visual inspection of ground-based images (Zwicky & Zwicky 1971), Sargent (1967) reported a faint spiral structure. However, its optical morphology is still not clear showing an elliptical shape with some peculiarities (Hansen, Jorgensen, & Norgaard-Nielsen 1987) and could be a merger remnant galaxy (Moles et al. 1988). Spectroscopic analysis has shown that 3C 120 presents a rotation curve most likely indicating the presence of an undetected disk (Moles et al. 1988). Based on this result, 3C 120 is normally quoted as an early-type spiral or S0 galaxy (Moles et al. 1988).

Although Seyfert galaxies are generally considered as radio-quiet objects, 3C 120 is an active radio-loud source showing a superluminal one-sided jet that extends $\sim 25''$ out of the core (Readhead et al. 1979; Walker et al. 1988; Walker 1997). Different authors (e.g. Baldwin et al. 1980; Pérez-Fournon et al. 1986; Soubeyran et al. 1989; Hua 1988) reported the existence of several continuum and emission line dominated structures in this object. Some of these structures have a clear relation with the radio-jet. Hjorth et al. (1995) detected a continuum dominated optical counterpart of the radio-jet using deep broad-band ground based images. On the other hand, an EELR (E_1) associated with the jet was found at $\sim 5''$ west of the nucleus (Hua 1988; Axon et al. 1989; Sánchez et al. 2004a). The nature of the remaining structures is still unclear (e.g. Pérez-Fournon et al. 1986; Moles et al. 1988).

This paper compiles data from IFS optical observations of 3C 120 using the optical fibers system INTEGRAL covering a central region of $\sim 16'' \times 12''$ field-of-view. We combined our

IFS data with high-resolution Hubble Space Telescope (HST) images. We describe the optical fibers instrument, observations, and data reduction in section §2. In section §3, we describe the emission line profiles in the circumnuclear region of 3C 120 and we present 2D spectra diagrams for different emission lines (appendix A). In the following sections, we present the stellar morphology and the structures detected (section §4.1), the average colors of the galaxy and the colors of those structures (section §4.2), and the emission-line morphology and ionization structure (section §4.3). In section §5, we apply a new technique to separate the spectra of different components coexisting in 3C 120 and analyze the properties of each component. We present the velocity field of the central region of 3C 120 and the discussion of several kinematic perturbations in section §6. A distance of 198 Mpc is assumed for 3C 120 throughout the paper (H_0=50 km s^{-1} Mpc^{-1}) which corresponds to a scale of $\sim$ 1kpc/$''$.

2. Experimental Set-Up, Observations, and Data Reductions

2.1. Integral Field Spectroscopy

IFS optical observations with fibers are based on the idea of connecting the focal plane of the telescope with the spectrograph slit using a fiber bundle. In this way, when an extended object is observed, each fiber receives light coming from a particular region of the object. Each individual spectrum appears well separated on the detector and therefore, spatial and spectral information are collected simultaneously. The wavelength limitations essentially depend on the characteristics of the spectrograph itself. The spatial resolution depends on the fiber sizes and the prevailing seeing conditions during the observations. The spatial coverage of fiber systems is relatively small (see LeFevre et al. 2003, for a counter example), but they are very useful when studying small size objects, such us the circumnuclear region of nearby active galaxies (e.g. García-Lorenzo, Arribas, & Mediavilla 2001), blue compact dwarf galaxies (e.g. Cairós et al. 2002) or gravitational lenses (e.g. Motta et al. 2002; Wisotzki et al. 2003).

IFS of 3C 120 was obtained the 26th of February 2003 at the Observatorio del Roque de los Muchachos (ORM) on the island of La Palma, Spain. The 4.2m William Herschel Telescope (WHT) was used in combination with the fiber system INTEGRAL (Arribas et al. 1998, 1999; Mediavilla et al. 1998) and the WYFFOS spectrograph (Bingham et al. 1994). The observations were carried out under photometric conditions and an average seeing of $1\farcs2$. The standard bundle 2 of INTEGRAL was used during these observations. This bundle consists of 219 fibers, each one with a diameter of $0\farcs9$ projected on the sky. A central rectangle is formed by 189 fibers covering a field-of-view of $16'' \times 12\farcs3$, and the remaining 30 fibers form a ring with a diameter of $90''$. Figure 1 illustrates the actual distribution of

the science fibers on the focal plane.

The WYFFOS spectrograph was equipped with a 300 groove mm^{-1} grating centred on 5500 Å (spectral coverage: 3500-9000 Å). A Tek6 CCD array of 1124 × 1124 pixels of 24 μm size was used, giving a linear dispersion of about 3 Å $pixels^{-1}$. With this configuration, and pointing to the central region of 3C 120, three exposures of 1800 seconds each were taken. The data were reduced using IRAF standard routines (Tody 1986). Although the reduction of IFS data from fiber-based instruments does not differ significantly from standard spectroscopic data reduction, we describe briefly in this section the reduction procedure.

A master bias frame was built by averaging different bias frames taken along the night. This bias frame was then subtracted from the science frames. In observations with optical fibers, flats-fields are obtained illuminating the focal plane uniformly, and obtaining spectra (the so-called flat-spectra). Thus, for a particular wavelength, the differences in response among fibers dominate the flat-spectra shape. These differences are due to their distinct focal-ratio degradation, position at the entrance of the spectrograph, etc. In this way, flat-spectra are used to homogenize the response of all the fibers. Flat-spectra are also used to obtain the polynomial fits to define the fiber path along the detector and extract the individual spectra from the whole image. Each spectrum appears well separated on the detector, with a width of approximately two pixels in the spatial direction (according to the core fiber image size of the fiber bundle used for these observations). The trace and extraction of individual spectra was performed using the standard routine APALL of IRAF. After this operation, frames of 1124 × 1124 pixels were reduced to 1040 × 219 pixel: each pixel in the spatial direction contains the spectrum of each particular fiber, a total of 219 fibers.

The wavelength calibration was done using the IDENTIFY and REIDENTIFY routines of IRAF. In order to carry out this procedure, we selected several isolated and well-distributed arc lines. Although it might be difficult to determine the actual uncertainty produced by the wavelength calibration, we have used the sky lines in our spectra to estimate the final wavelength errors, being smaller that 35.5 kms^{-1} and 29.5 kms^{-1} at blue and red wavelengths, respectively.

The SP1045+378 flux standard star (Isaac Newton Group Database) was observed the same night and under similar conditions as for 3C 120. The standard star has been used to calibrate a flux ratio by comparing with the standard-star flux tables of Stone (1977). We reduced the SP1045+378 frames in a similar way than the object ones, correcting them for differential atmospheric refraction (Filippenko 1982) using E3D (Sánchez 2004). Then, we extracted the observed spectrum of the star by co-adding the spectra of the central 37 fibers, which includes >99% of the total flux. Comparing this observed spectrum with the flux-

calibrated spectrum of SP1045+378 we derived a sensitivity curve that we used to calibrate the object frames.

We combine the IDA tool (García-Lorenzo, Acosta-Pulido, & Megias-Fernández 2002) and the Euro3D visualization package (Sánchez 2004) to analyze the data and generate two-dimensional maps of any spectral feature (intensity, velocity, width, etc). Maps recovered from spectra are images of 51×37 pixels with a scale 0.″3/pixel. While the spatial sampling of the used INTEGRAL configuration is 0.″9 (that is, the fiber diameter of the bundle 2), the centroid of any peak in our maps can be measured with an accuracy of around 1/5 of the fiber diameter, that is $\sim 0.''2$ (e.g. Mediavilla et al. 1998).

2.2. HST imaging

Wide-Field Planetary (WFPC) camera images of 3C 120 in different bands are available on the archive of the Hubble Space Telescope (HST). We obtained these images to study the morphology of this object. Table 1 summarizes the properties of these images. The data set comprises three broadband images (F555W, F675W and F814W), which roughly corresponds to the standard V, R and I-bands, and a medium band image (F547M). These images basically sample the continuum emission in 3C 120, since the equivalent width of mostly all the emission lines is very small compared with the width of the bands. However, there is a non neglectible contamination, dominated by the [OIII] and Hβ emission lines in the F555W-band image (and Hα in the F657W-band image). The F547M-band image can be used as an estimation of the pure continuum emission, since the emission lines are at the edge of its transmission curve. The data set is deep enough to study the different structures present in this object (Soubeyran et al. 1989).

3. Atlas of Spectra

Figure 2 shows the nuclear spectrum of 3C 120 in the full wavelength range. This spectrum has been obtained by co adding the seven spectra closest to the continuum peak. This is almost equivalent to a hexagonal aperture of 1.″6 in radius centred at the optical nucleus of 3C 120. We can easily recognize several emission lines and the characteristic broad component of permitted emission lines of Seyfert 1 galaxies.

In the Appendix A, we present the individual spectra corresponding to each of the different observed positions (fibers) in selected spectral intervals that include the most important emission lines (spectra diagrams).

3.1. Emission-Line Profiles

The profiles of the emission lines in the nuclear spectrum of 3C 120 show a considerable blending due to the wings of the broad component of permitted lines (Fig. 2). The Hδ profile appears to be considerably broader than any other Balmer line, but this is not the case of Hδ as in previously found by other studies (Phillips & Osterbrock 1975; Baldwin et al. 1980). The HeIλ5876 shows also a considerable broadening. At this step, we cannot discuss the origin of these features in terms of recombination models and reddening effects because the nuclear spectrum in figure 2 includes the contribution of the nucleus and the surrounding galaxy. In section §5 we separate both contributions and we will be in position to tackle this discussion. The low spectral resolution of the current IFS data prevents the detection of double peaks reported by Axon et al. (1989). However, the emission lines show asymmetric profiles in some locations outside the central region.

4. Data analysis and results

4.1. Broad band distribution and morphological structures.

Broad-band images of 3C 120 were recovered from our IFS data by coadding the flux in spectral ranges that mimic the band-passes of the previously refereed HST images and using an interpolation routine (Sánchez 2004; García-Lorenzo, Acosta-Pulido, & Megias-Fernández 2002). The specific wavelength ranges for each band were 3900-4900 Å(B-band), 5000-6000 Å(V-band), 5600-5700 Å(V'-band), 6100-7100 Å(R-band) and 7550-8550 Å(I-band). All images show a bright nucleus on top of a weak host galaxy. Figure 3A presents the intensity map corresponding to the V-band filter. The intensity contours have an elliptical shape except for those at around 4 arcsec from the central peak, showing an elongation toward the west. There are remarkable similarities between the restored map (Fig. 3A) and the F555W-band image from the HST (Fig. 3B), despite of the differences in wavelength ranges and spatial sampling. The superior resolution of the HST images allows to directly detecting several structures. These structures have been previously reported subtracting a galaxy template to broad and narrow band ground base images (e.g. Baldwin et al. 1980; Pérez-Fournon et al. 1986; Hua 1988; Soubeyran et al. 1989). We have labeled, using the nomenclature introduced by Soubeyran et al. (1989), the different detected structures (figure 3B). The HST/F555W-band image allows to resolve them, showing a richer level of structures. In particular, structures B, and C are composed of a smoothed low surface brightness component and more luminous clumpy substructures. Structure A seems to be more collimated, as previously noticed by ground based imaging, which explains why it was initially

confused with the optical counterpart of the radio jet (e.g. Pérez-Fournon et al. 1986). It shows also a low surface brightness component and four clear clumps. We overplot in figure 3B the radio-map at 4885 MHz (Walker 1997), showing that the structure A is most likely related to the structure B rather than to the radio-jet. Indeed, the HST images suggest that both structures belong to a sequence of clumpy knots which are physically connected. Dust lines and shell structures not detected from the ground are seen in the inner regions. Two shell arcs at $\sim 1''$ north and south of the central peak are clearly detected in the HST images. Although previous HST images show extensions to the north-west and south-east in the inner region of 3C 120 (Zirbel & Baum 1998), to our knowledge this is the first time that the shell structure is clearly visible. The north and south shells are named S_N and S_S, respectively, hereafter. The S_S seems to be connected to structure A by a faint tail.

A 2D modeling of the broad-band images was performed using GALFIT (Peng et al. 2002) to obtain a clear picture of the morphology of 3C 120. This program has been extensively tested in the image decomposition of QSO/hosts (Sánchez et al. 2004b). The 2D model comprises a narrow Gaussian function (to model the nucleus) and a galaxy template (to model the galaxy) both convolved with a PSF. We performed the fit twice, first using a Sersic law (Sèrsic 1968) to characterize the galaxy and then using a de Vaucouleurs law (de Vaucouleurs 1948). This method allows us to determine the morphological type of the host galaxy, based on the obtained Sersic index, and to get a good determination of the galaxy flux, based on the modeling the de Vaucouleurs law (Sánchez et al. 2004b). The PSF was created using a field star for the analysis of the HST images, and a calibration star for the analysis of the broad-band images recovered from the IFS data.

We applied first the fitting technique to the HST images because of their better spatial resolution. The nucleus was saturated in the HST/F814W-band, which prevents us to do a two-model fitting, and limits the reliability of any morphological classification, which strongly depends on the shape of the profile in the inner regions. To derive a rough estimation of the host magnitude we masked the nucleus, and fixed the scale to the average of the values derived in the other available HST/bands. Further checks, explained below, demonstrated that this approach was valid. Table 2 summarizes the results from this analysis. For each band it shows the derived Sersic index, the nucleus and host magnitudes and the effective radius of the host galaxy. The derived Sersic indices, all near or larger than the nominal value of 4 for an early-type galaxy, confirm the morphological classification of the host galaxy of 3C 120 as a bulge dominated galaxy.

We subtracted the object template (galaxy+nucleus) derived by the 2D modeling from the original images, obtaining a residual image for each band. These residual images were used to study the properties of the different structures, once decontaminated from the smooth

component. As an example, the residual image of the V-band and the HST/F555W-band are shown in Figure 3C and 3D, respectively. The already quoted structures are now clearly identified. The S_S shell coincides with an extended emission line region (EELR) previously detected in this object (Hua 1988; Soubeyran et al. 1989; Sánchez et al. 2004a) and labeled as E_2 (Soubeyran et al. 1989).

4.2. Colors and gaseous distributions in 3C 120

As already quoted all the broad-band images recovered from the IFS data show a similar morphology than the V-band image shown in figure 3A. Combining these recovered broad-band maps, we obtained color maps of 3C 120. Figure 4A shows the $V-I$ color map derived from the IFS data. It shows a blue circumnuclear region elongated to the southwest. The elongation towards the west seen in the broad band images has also a counterpart in the color maps showing bluer colors at a region $\sim 4\farcs5$ west of the nucleus than its surroundings. Figure 4B presents the $V-I$ color map derived from the F555W and F814W-band HST images. Despite of their different spatial resolution, figures 4A and 4B present remarkable similarities. The different structures quoted in section §4.1 show bluer $V-I$ colors than the average color of the host galaxy, as already noticed (e.g. Fraix-Burnet et al. 1991). Figure 4B also shows evidence for two weaker shells farther from the central peak than S_N and S_S but also at the north and south. However, these "secondary" shells are fainter, being at the detection limit.

Both the V-band and the F555W-band images are contaminated by the emission from [OIII] and Hβ. A rough estimation of how strong that contamination is can be obtained by subtracting a scaled continuum image, clean of those contaminations. Figure 4C shows the residual image of the INTEGRAL V-band image after the subtraction of an adequate continuum (the V'-band image). A similar estimation was done for the HST images, subtracting the continuum dominated F547M-band image from the F555W-band image (Figure 4D). This image was smoothed using an 11×11 pixels median kernel to increase the signal-to-noise ratio. The resulting maps are a rough estimation of the distribution of the [OIII]+Hβ emission. The position of two of the EELRs detected in this object (E_1 and E_2, hereafter) is indicated (Soubeyran et al. 1989; Sánchez et al. 2004a). The residual images of the continuum, after subtracting a model template (Fig. 3C and 3D), are overplotted for comparison purposes. The S_N and S_S shells show a strong gaseous emission in the HST images, which in the S_S extends towards the E_2 region.

Figure 5 shows the $V-R$ colors of the host galaxy and the different structures as a function of the $R-I$ colors. As already noticed in the color image, the structures have

bluer $V-R$ colors than the host galaxy. This indicates most probably the presence of somewhat younger stellar populations associated with them. However, they show a wider range of $R-I$ colors than that of $V-R$ colors. Indeed, the average $R-I$ color of the host galaxy is within the range of $R-I$ colors of the different structures. The color-to-color distribution derived from synthetic models has been included in the figure for comparisons. The discontinuous line shows the colors of single stellar populations calculated using the Bruzual & Charlot (2003) models. We assumed a solar metalicity and a Chabrier (2003) IMF. The labels indicate the logarithm of the stellar population ages in Gyrs. In general terms, the color-to-color distribution does not match with that simple model, apart from the case of the S_N and S_S shells. For the remaining structures, the $R-I$ colors correspond on average to a young stellar population of $\sim 6\times10^8$ Gyr, but the $V-R$ colors correspond to older stellar populations. This may indicate that the real populations are a composite of populations. The dotted line shows the colors of different galaxy types (E, Sab, Sbc, Scd and Irr) (Fukugita et al. 1995), which mainly correspond to different mixes of stellar populations. The $R-I$ color of the host galaxy mainly corresponds to a Sab-Scd galaxy. On average, the structures have $V-R$ colors that correspond to the same kind of galaxies (Sab-Scd), but their $R-I$ colors expand over all the range of possible colors.

So far we have ignored the effects of dust in the color-to-color distribution shown in Figure 5. However, the dust content in 3C 120 is rather high; an average value of $A_V \sim 4$ mags has been estimated (Sánchez et al. 2004a). Dust extinction redden both $V-R$ and $R-I$ colors in an almost similar way (Fitzpatrick 1999). The effects of dust in the color-to-color distribution is illustrated with an arrow in Fig. 5. It is clear that the dust is not homogeneously distributed in the galaxy: e.g., typical dust lanes are seen in figure 3B. A combined effect of different stellar populations and a non-homogeneous distribution of dust could explain the observed color-to-color distribution. In that case, the S_N and S_S structures would be dust-free areas dominated by a single stellar population.

However, results from broadband colors should be taken with care. The contamination of broadband filters by strong emission lines can drastically affect the morphology of color maps. In the case of 3C 120 the problem is even worse because of the contribution and contamination from the broad component of the Balmer emission lines in the central regions.

4.3. Line-Intensity Maps and Ionization Structure

We performed a line profile fitting and de-blending in order to study the integrated high and low ionization gas distribution, their physical properties and kinematics. We fit a single Gaussian to any of the bright emission lines in the spectra. For the Balmer lines, we included

a second broader Gaussian to fit the wide line from the broad line region (BLR). In spite of our poor spectral resolution, we found that several spectra have evidence of substructures, showing asymmetric profiles with blue or red wings indicating the presence of several gaseous systems in 3C 120. Indeed, previous authors (Axon et al. 1989) reported the existence of several components in the emission lines of 3C 120, but to apply a line-profile decomposition to separate the different gaseous components would be unrealistic because of the low spectral resolution of the current IFS data. The broad component of the Balmer lines is confined to the nucleus discarding an extended broad emission line region.

Figure 6 shows the intensity maps of [OIII]λ5007 (figure 6A) and Hα (figure 6B) after the deblending. Intensity contours of ionized gas are clearly elongated toward the E_2 structure. Emission line maps present an elongation to the west, forming a clear secondary peak at around 5 arscec from the nucleus in the [OIII] intensity map. This secondary peak corresponds to the E_1 structure previously quoted (section §4.2). The ratio of the Hα intensity of the nucleus and E_1 is much smaller than that of [OIII]λ5007, suggesting a high ionization nature of the latter. The nuclear region shows a low ionization degree in the [OIII]λ5007/Hβ map surrounded by a ring of high ionization (figure 6C), with larger values at the south of the nucleus, coincident with the location of E_2. A high ionisation region expands from the ring to the west, increasing the ionisation degree along this direction. The [NII]λ6584/Hα line ratio map (figure 6D) also shows a ring structure, surrounding the nuclear region. The E_1 is on the path of the 3C 120 radio-jet, as well as the continuum dominated structure *A*.

The high [OIII]/Hβ ratio of E_1 (figure 6C) discards a relation between *A* and E_1, assuming that *A* is a star forming region in a spiral arm or a tidal tail, and points, more likely, to a direct connection between E_1 and the radio-jet (Sánchez et al. 2004b). While the nucleus and the *A* region present [OIII]λ5007/Hβ and [NII]λ6584/Hα ratios at the limit of HII regions in a diagnostic diagram (Veilleux & Osterbrock 1987), those ratios of E_1 and its west surroundings are placed on the high-ionization region .

The distribution of the Hα/Hβ line ratio (figure 6E) shows a dust lane crossing 3C 120 along the southeast-northwest direction. The high Balmer decrement at the west points to a high dust obscuration around E_1. However, we cannot rule out that the high Hα/Hβ ratio may be related to the low signal to noise of the narrow component of Hβ in the circumnuclear region of the galaxy. The electronic density derived from the [SII]λ6716/λ6730 presents a patchy structure, showing an enlargement in the location of E_1. In the next section, the ionization conditions of the different structures in the observed region of 3C 120 are studied in detail.

5. Decoupled spectra of the different components in 3C 120

In the previous section, we used the traditional method (Gaussian fitting) to deblend the different gaseous components. IFS optical observations record spatial and spectral information simultaneously. Taking advantage of this fact, we have developed a technique (3D-modeling hereafter) to disentangle the spectra of the main components of 3C 120 (nucleus+host), and to obtain cleaned spectra of the different structures described above. This technique has been successfully applied recently (Sánchez et al. 2004a). A brief summary of the technique is described in the Appendix B, and will be explained in detail in a separate article (Sánchez et al., in prep.). In summary, the technique provides us with a spectrum of each of the main components of the object plus a residual data cube that can be used to derive cleaned spectra of the different structures in the object and/or analyze their morphological and kinematical properties. This is an extension of the 2D modeling of images applied in section §4.1 to each of the monochromatic images of the data cube derived from IFS optical observations. We applied the 3D modeling to the current data and we derived the 3C 120 nucleus spectrum, the mean host galaxy spectrum and a residual data-cube of spectra.

5.1. Morphological structures from the residual data cube of spectra

To compare the results from the proposed technique to those of the traditional method, figure 7A shows the greyscale of the residual from the 2D modeling of the F555W/HST-band image obtained in section §4.1 (figure 3D). We over plotted the contours of a narrow-band image centred on the continuum adjacent to the [OIII] emission line (5204-5246 Å) extracted from the residual data cube of spectra obtained after the 3D modeling. The main continuum dominated structures (A, B and C) are detected $\sim 1''$ from the nucleus. As expected, the shell structure detected at $\sim 1''$ north and south of the nucleus in the HST images is not detected with the IFS data. A combination of the superior resolution of the HST images, the effects of the seeing and the sampling of our IFS data can explain it. In figure 7B we present the greyscale of the F555W−F547M image (obtained in section §4.2, figure 4D) and the contours of a narrow-band image centred on the [OIII]λ5007 emission line (5170-5200Å) extracted from the residual data cube. As we quoted above (section §4.2), the F555W-F547M image is a rough estimation of the [OIII]-Hβ emission map. Although both images are in good agreement, integral field spectroscopic data are more adequate to detect extended emission line regions (EELRs) that are diluted in broadband filter images, like the F555W-band one. It is possible to identify the E_1 and E_2 structures, and a third region (E_3 hereafter) at the north-west of the F555W-F547M image. Soubeyran et al. (1989) already detected these

emission line regions, using narrow-band imaging centred on the [OIII] emission line spectral region. E_1 and E_2 are completely coincident with their reported positions. The peak of E_3 found by Soubeyran et al. (1989) is not included within the field of view of INTEGRAL. We are confident of our detection, and most probably we are seeing a tail previously not detected of E_3 towards the nucleus.

5.2. Spectra of the nucleus and the host galaxy

Figure 8 and 9 show the spectra of the different deblended components of 3C 120. Figure 8A shows the spectrum of the nucleus. Its continuum follows roughly a power-law with a slope of $\alpha \sim -0.5$ ($F_\lambda \propto \lambda^\alpha$). It contains broad-emission lines, without any trace of them in the spectrum of the host galaxy (figure 8B), which indicates that the decoupling technique has worked properly. The intensities of the narrow emission lines is weaker in the nucleus than in the host galaxy spectrum. Indeed, many emission lines are clearly detected in the host galaxy spectrum but not in the nucleus.

To derive the properties of the emission lines in the spectrum of the nucleus, we fit Gaussian functions to the different emission lines. The adjacent continuum was modelled with a low-degree polynomial function. To increase the accuracy of our model, different nearby emission lines were fitted together, defining line systems with the same systemic velocity and full-width-half-maximum (FWHM). After several attempts, the best (and simplest) modeling was obtained including two decoupled broad systems, with $\sim$8796 km s^{-1} and $\sim$2188 km s^{-1}, and a narrow system, with $\sim$700 km s^{-1}. Recently, Ogle et al. (2004) also reported two broad and one narrow component for the H-Balmer lines in the nucleus of this galaxy with a similar velocity dispersions than those derived here. Table 3 lists the result from the fit, including the wavelength, the flux and their 1σ errors for each detected line. The uncertainties in the determination of the flux of the narrow emission lines affected by line blending are high as expected. The Hα/Hβ line ratios are in the range of $\sim$3.0-3.6 for the different line systems, in agreement to the nominal values for case B recombination (Osterbrock 1989). Therefore both the narrow and broad emission line regions are not significantly affected by dust, as expected for a type 1 AGN nucleus. We estimated an effective temperature of $\sim 2.3\times10^5$ K using the ([OIII]λ5007+[OIII]λ4959)/[OIII]λ4363 line ratio and the relation between this ratio and temperature (Osterbrock 1989) typical of this kind of AGN.

Figure 8B shows the average spectrum of the host galaxy together with the spectra of different synthetic models consisting on single stellar populations of different ages. We used the Bruzual & Charlot (2003) models, assuming a solar metallicity and a Chabrier

(2003) initial mass function (IMF). The effects of dust were included in the model using the extinction curve of Fitzpatrick (1999) for a dust absorption of A_V ∼4 mags (the average value in the host galaxy, as we will show below). Two extreme cases were plotted, representing an old (∼16Gyr, red line) and a young stellar population (∼0.01Gyr, blue line). These extreme cases are a clear over simplification, but they can be used just for qualitative comparisons. A single stellar population cannot describe the observed spectrum: the optical slope between λ ∼5000 Å and λ ∼6500 Å matches well with that of an old stellar population. However, the slope at larger wavelengths is flatter, more similar to that of a young stellar population. We already noticed it (section §4.2) when we analyzed the broadband colors of the host galaxy (Figure 5). Only a mix of different stellar populations can explain the observed spectrum.

We included in figure 8B the spectrum of a fifty-to-fifty mix of both components (orange line). Even this simple model can describe quite well the spectrum of the host galaxy for λ >4500Å. At shorten wavelengths there is an increase of the flux, which does not match with the mix model (dashed line). It is well known that powerful radio galaxies show a significant blue-UV excess (Lilly & Longair 1984) most probably due to scattered light from the nucleus than to young stellar populations (McCarthy et al. 1987). This scattered light can be well described by a power-law. Adding a power-law to the mix model we can describe the average host galaxy spectrum for any wavelength (orange solid line). Therefore, three components are needed to explain qualitatively the spectrum of the host galaxy: (a) an underlying old stellar population, (b) a young stellar population, and (c) a nebular continuum, most probably scattered light from the nucleus. We did not perform a proper fitting to determine the best fractions of the different components because it would not change the qualitative statement, and, in any case, the specific fractions will depend on the assumed synthetic models for the young and old populations and we chose them arbitrary. The contribution of each component to the total flux are ∼5% (a), ∼55% (b) and ∼40% (c) at 4500 Å and ∼35%(a), ∼64% (b) and ∼2% (c) at 6000 Å. Similar results have been found in the study of other powerful radio galaxies (e.g. Tadhunter et al. 1996).

Table 3 lists the results derived from fitting a single Gaussian to the emission lines in the host galaxy spectrum. As we quoted above, only narrow emission lines corresponding to a dispersion velocity of FWHM∼700 km s^{-1} are detected. These emission lines are considerably stronger than the narrow-emission line region in the spectrum of the nucleus, indicating the presence of an extended narrow-emission line region which extends through most of the field of view. Similar results have been found in spectroscopic studies of radio-quite type 1 AGNs (e.g. Jahnke 2002; Jahnke et al. 2004). The Hα/Hβ line ratio is ∼10, indicating a dust absorption of A_V ∼4 mags when comparing with the nominal case B recombination value (Osterbrock 1989) and using the Fitzpatrick (1999) extinction curve. In average the host galaxy contains a rather high dust content, but the dust distribution is

not uniform as we can see in figure 6E. We estimated an effective temperature of ∼14000 K using the ([OIII]λ5007+[OIII]λ4959)/[OIII]λ4363 line ratio and an electron density of n_e∼10 cm^{-3} using the [SII]λ6716/6731 line ratio. To derived these quantities, we used the relations between these line ratios and the measured parameters (Osterbrock 1989). The line ratios log([OIII]λ5007/Hβ)∼1.2 and log([NII]λ6583/Hα)=−0.4 indicate most probably a direct photo ionization by the UV flux from the AGN, consistent with the result shown in Section §4.3.

5.3. Spectra of the EELRs: Origin of the ionization

The integrated individual spectra of the structures E_1, E_2, E_3 described in section §5.1 were extracted from the residual data cube. Figure 9A presents the spectra of each EELRs (E_1, E_2, E_3), which are remarkable similar. They have a clear gaseous nature, without appreciable continuum emission. This result confirms that the continuum dominated structure *A* is not related to E_1 as we pointed out in section §4.2. A visual inspection of the relative strength of the different lines indicates that the dominant ionization source is the AGN or shocks, rather than a star formation process. This was already noted in section §4.3 and figure 6C for E_1, and E_2. Table 4 lists the result of the Gaussian modeling of the emission lines in these spectra. Different line ratios and parameters derived from them are listed in Table 5. We included the [OIII]λ5007/Hβ, [NII]λ6583/Hα, [SII]λ6716/[SII]λ6731 line ratios, and the derived dust absorption (A_V), electron density (n_e) and effective temperature (T_{eff}). Those values of the nucleus and the host galaxy spectra were also included for comparison purposes. As we already mentioned, the ionization conditions are similar in the different EELRs, being also similar to those of the nucleus and the host. Figure 10 shows the classical diagnostic diagram of the [OIII]λ5007/Hβ line ratio as a function of [NII]λ6583/Hα for the different components of 3C 120, including the division between AGNs and star forming regions (Veilleux & Osterbrock 1987). The major difference is found in the position of the nucleus in the diagram, which seems to lie in the location of star forming regions. This is most probably due to the large uncertainties in the [NII]λ6583/Hα line ratio derived for the spectrum of the nucleus, largely influenced by the deblending process of the narrow and broad emission lines, as we quoted above. The derived effective temperature (T$\sim 1.4 \times 10^4$ K) for the host galaxy spectrum does not exclude the hot stars as a possible origin for the ionization but the high [SII]/Hα, [NII]/Hα, and [OIII]/Hβ ratios indicate that the average ionization for the host is the AGN or/and a shock process. i.e., the observed spectra cannot be found in HII regions. The [NII]λ6583/Hα line ratio of the E_3 region is lower than that value for the rest of the structures. E_3 is the faintest detected EELR and it was not completely covered by our field-of-view, according to the [OIII] maps shown by Soubeyran et al. (1989). Its

spectrum is noisier and with some clear defects at specific wavelengths produced by the modeling technique. A detailed inspection of the spectrum shown in Fig. 9 shows that the [NII]λ6583 line is distorted by one of these defects, affecting the [NII]λ6583/Hα line ratio, which error is clearly larger than the formal error plotted in Fig. 10. Despite these caveats, it is clear that star formation processes do not dominate the ionization of the different EELRs.

The dust content in the EELRs is lower than the mean obscuration of the host. In particular, for the E_2 and E_3 regions the dust absorption is almost half of the average in the host galaxy. On the other hand, the electron density in those clouds is $\sim$10 times lower than the average. However, this density is $\sim$10 times higher in the E_1 region, i.e. $\sim$100 times larger than in the other clouds. This indicates most probably a different origin of those clouds. In Sánchez et al. (2004a) we discussed in detail the nature of the E_1 emission line region. It is most probably associated with the radio jet that crosses this cloud, compressing it due to its lateral expansion, and splitting it in two different kinematics regions (Axon et al. 1989; Sánchez et al. 2004a). The compression is reflected in the increase of the electron density. The nature of the ionization is not clear in this cloud, since a post-shock zone can also give rise to the observed line ratios. The similarities between the line ratios for the different EELRs, and between them and the host galaxy ones, may indicate a similar origin for the ionization. That is, direct photo ionization from the UV-field of the AGN. In that case the effect of the jet over the E_1 would be reduced to a split of the cloud and a compression that give rise to a density enhancement.

5.4. Spectral energy distribution of the continuum dominated condensations

Figure 9B shows the spectral energy distribution (SED) of the continuum dominated structures A, B and C detected in 3C 120 within the field-of-view of our IFS data. The SEDs were obtained by an average of the integrated spectra of the different structures extracted from the residual data cube over spectral ranges of 300Å width. The low intensity of the continuum dominated structures and the subsequent low signal-to-noise prevents us of using directly the extracted spectra for this analysis. The SEDs were cut at 7500Å since at larger wavelengths the imperfect subtraction of the sky-lines and the noise enhancement strongly affect the reliability of the derived SED. Synthetic spectra for three different stellar populations of different ages were included for comparison purposes. These spectra are similar to those shown in the figure 8B (described in §5.2), but without including the effects of dust. The SEDs are almost flat in the plotted ranges, being roughly consistent with a mix of a young stellar population with an underlying old stellar population. This result agrees with the results based on the broadband colors of the structures, discussed in §4.2. Therefore,

the continuum structures are experiencing a decrease of the dust content, rather than an increase of the star formation. This seems to be particularly valid for the A structure, which lies in a minimum of the dust content, derived from the Hα/Hβ line ratio (See Fig. 6E). Unfortunately, we cannot check it for the B and C structures, because the gaseous emission in those regions is less luminous and therefore the Hα/Hβ ratio is uncertain.

So far only starlight was considered to explain the emission found in the different condensations. However their SEDs could be also explained considering other components, like scattered-light from the nucleus and/or synchrotron emission associated with the radio-jet. Hjorth et al. (1995) detected polarization in the condensation A, which direction and magnitude were consistent with those found by Walker et al. (1987). This may indicate a connection between that condensation and the radio jet. Indeed, it may indicate that condensation A consists, at least partially, of optical synchrotron emission. However, as it was shown in §4.1 (and noticed by Hjorth et al. 1995), A does not follow the radio-jet into the core, being more likely associated with B and C. Furthermore, the measured polarization may be due to unsubtracted scattered-light from the nucleus (Hjorth et al. 1995), that we detected in the average spectrum of the host (Fig. 8 and §5.2). Indeed, the SEDs of the three different condensations do not differ significantly (Fig. 9B), and, in particular, they show almost the same $V-R$ colors (Fig. 5), which indicates, most probably, a similar origin for all of them. Since most of the scattered-light has been removed and the synchrotron radiation could also contaminate A, these condensations are most probably dominated by starlight.

6. 3C 120 Velocity Field

The central wavelengths of the Gaussians fitted to the individual spectra (section §4.3) give us the radial velocity associated to the ionized gas at each position. Interpolating the individual emission line centroids, we obtain the velocity field of different emission lines. Uncertainties due to wavelength calibration (< 35 km s^{-1}) and those related to the fitting process (~ 15 km s^{-1}) are small enough to be irrelevant for the following discussion.

Figure 11 shows the velocity field of the ionized gas derived from [OIII]λ5007 and Hα lines. While Hα traces the kinematics of low ionisation gas that describe the general pattern of the galaxy, [OIII] draws the signatures of high ionization gas, characterizing the most perturbed regions. Previous kinematics studies of 3C 120 found a rather chaotic velocity field (Baldwin et al. 1980) and some slight evidences of a co-existing rotating system (Baldwin et al. 1980; Moles et al. 1988). Despite of the different spatial resolution and coverage of the IFS data in this paper, our results are in agreement with those of Baldwin et al. (1980) and

Moles et al. (1988) pointing towards highly distorted kinematics in this object.

The unclear morphology and highly distorted gas kinematics of 3C 120 makes a simple interpretation of the velocity structure difficult. The ionized gas velocity field presents a general regular pattern, with larger velocities at the north-west and lower at the south-east that may be consistent with a disk rotating around an axis along the north-east direction (figure 11A and 11B). Several kinematical perturbations can be identify in the velocity maps as well as a regular rotation.

A velocity gradient is located at $\sim 5''$ west of the nucleus, aligned with the radio-jet (figure 3B), at the position of E_1 (figure 11A). Using a better spectral resolution, Axon et al. (1989) show that there are two different kinematics components rather than a velocity gradient. The north component is receding while the south component is approaching. The kinematical perturbation is most probably due to the lateral expansion of the radio-jet (Axon et al. 1989): as already quoted, the interaction of the radio-jet and the intergalactic gas produces an enhancement of the gas density (section §4.3), and perturbs the kinematics (Sánchez 2004).

The velocity field derived from [OIII] is much more distorted to the east (farther than 4 arcsec from the nucleus) than that one derived from Hα. Although the signal to noise in the IFS spectra is low and uncertainties are larger in that region, differences in the kinematics may be explained by the different origin of these lines. The comparison of the continuum dominated structures and the velocity field derived from the Hα shows that A and B coincide with a velocity distortion located at the west of the nucleus (figure 11B). This kinematical feature is similar to those found in the velocity field of spiral galaxies because of the arms (e.g. Knapen et al. 2004). This gives support to the idea of identifing the A and B regions as structures in an spiral arm in 3C 120 in spite of its poor gas content and continuum emission dominated by starlight. We will discuss in detail the origin of this arm-like structure in section §7.

The comparison of the ionized gas structures E_2, and E_3 (figure 7B) and the velocity field gives clues to the origin of the EELRs (figure 11C). The morphology of E_3 follows remarkably well an east-west gradient in the velocity map. E_2 is in a close to constant velocity region. Both clouds are in regions which present strong kinematical perturbations from the canonical rotation. These perturbations are more prominent in the velocity structure of the high ionization gas than that of the low ionization gas.

Fitting a single Gaussian to the emission lines in the residual data cube of spectra (section §5), we have derived the velocity behavior of the E_1, E_2, and E_3 residual structures. Figure 11D shows the velocity map derived from the [OIII] lines in the residual spectra.

We will refer to this map as the velocity map of residuals hereafter. The kinematics of the structures trace remarkable well the perturbations in the velocity field, although their kinematical features are smoother in the latter. The smoothing is a clear consequence of the blending of the host galaxy and the structure spectra. The velocity map of the residuals represents much better the kinematics of the gas clouds in E_1, E_2, and E_3. We found a clear gradient of velocities in the region corresponding to the three structures pointing to inflows/outflows of gas at different inclination angles and outside of the galactic disk. While regions E_1 and E_2 present a north-south velocity gradient, E_3 shows an east west gradient in good agreement with the [OIII] velocity map (figure 11A).

Despite of the bulge dominated morphology found in the inner regions of 3C 120, the velocity field derived from Hα indicates the presence of a rotating disk along the north-west/south-east (figure 11B). In that case, the receding velocities at the northwest suggest that southeast is the face closer to the observer. The velocity gradient also traces the line of zero velocities, but it is not clearly defined in the derived velocity field because of the distortions in the center introduced by the Sy1 nucleus. With a larger spatial coverage, Baldwin et al. (1980) determined a PA=$72^\circ \pm 15^\circ$ for the minor kinematics axis. This angle agrees with the semi-minor axis determined from the 2D modeling of the galaxy (section §4.1). A visual inspection of the velocity fields in figures 11A and 11B indicates that this PA may be a good estimation of the minor kinematics axis, when considering the distortion at the west. However, this distortion is most likely produced by the interaction of the radio-jet with the E_1 cloud (Sánchez 2004), and most probably is not related with the rotating disk. The isovelocity contours of the velocity field derived from Hα and the position of the kinematical center ($\sim$ 0.8" north-west of the nucleus) suggest that the minor kinematical axis is most likely along PA$\sim 50^\circ$, which is not far from the photometric determinations and within their uncertainties. Therefore, we will consider hereafter a PA=-40° for the major kinematics axis of 3C 120.

Figure 12 shows the rotation curve of 3C 120 derived from the velocity field of Hα, assuming a PA of -40° for the major kinematics axis. This curve is clearly distorted at the south-east due to the kinematical perturbations associated with E_2. However, the north-west portion of the curve is remarkable similar to those of galactic rotating disks (Binney & Merrifield 1998). The effects of the perturbations in the south-east portion of the curve must be removed prior to model the 2D distribution of the rotating component of the galaxy. For doing so, it was assumed that the approaching portion of the rotation curve (south-east) follows a symmetrical counterpart of the receding portion (north-west). This *hypothetical* rotation curve was included in Figure 12. This curve was then used to derive a template of the velocity field by applying a simple rotational model (Mihalas & Binney 1981), for different inclinations varying from $\sim 5^\circ$ to $\sim 85^\circ$. Subtracting those templates from the Hα

velocity field and minimizing the differences at the northwest region (where the rotation curve really corresponds to the 3C 120 kinematical behavior), we estimated an inclination angle of $\sim 40^\circ$ for the disk component of 3C 120. The velocity field template corresponding to that inclination angle is shown in figure 11E. This estimation of the inclination is in agreement with the determination from the external isophote (Moles et al. 1988). As quoted before, the internal isophotes are less elongated and distorted at the west than the external ones. This suggests a different inclination angle, smaller at the inner than at the outer regions. Indeed, the ellipticities derived from the 2D modeling (section §4.1) indicate that the inclination may range from $\sim 20^\circ$ to $\sim 43^\circ$ in the center, in agreement with the kinematical estimation. The differences in inclination from the center to the outer regions, although small, suggest a slightly warped disk component in 3C 120.

Figure 11F shows the residual of the [OIII] velocity map once subtracted the template shown in Fig. 11E (residual velocities hereafter). This residual map shows an almost flat area of 0 ± 20 km s^{-1}at the north-west region, within the uncertainties of the velocity determination. At the west, coincident with the path of the radio-jet and the location of E_1, there is a north-south gradient of ~ 148 km/s, in agreement with the results by Axon et al. (1989). At the location of E_2 there is a rather chaotic residual velocity structure, with velocities ranging from $\sim$270 to 460 km/s. A slight east-west gradient of ~ 32 km/s is found at the location of E_3. The residual velocities (Fig. 11F) and the velocity map of the residuals (Fig. 11D) present a rather good qualitative agreement in spite of the strong conceptual and practical differences of the two methods used to derived them. This supports the idea of the presence of a rotational component in 3C 120.

Due to the low spectral resolution of our data no attempt was done to analyze the velocity dispersion maps.

7. discussion

In previous sections we presented several aspects of 3C 120 that describe a puzzle environment. 3C 120 is morphologically speaking a bulge dominated galaxy, which contains a rotating stellar disk and several continuum- dominated structures and EELRs. We analyzed in detail those structures in order to determine their nature. The E_1 is caused by the interaction of the radio-jet with the intergalactic medium, as already discussed in Sánchez et al. (2004a).

The newly reported shells in the central region of 3C 120 is an addition to the complex picture of this object. Shells are common structures in elliptical and SO galaxies, although

a few number of spirals also show the presence of this kind of features (Malin & Carter 1983; Schweizer & Seitzer 1988). Although models considering internal shock waves were proposed to account for the presence of shells in galaxies (see e.g. Williams & Christiansen 1985) the most accepted idea is that they are generated by merging processes (see e.g. Hernquist & Spergel 1992, and reference therein). Numerical simulations indicate that the number and sharpness of shells in merger remnants depend on the mass ratio and the absence (or presence) of a central buldge in the progenitors (González-García & Balcells 2004). The radial distribution of shells depends on the potential of the host galaxy and their morphology can appear aligned or randomly distributed around the galaxy (Prieur 1990). 3C 120 shows two well defined shells, labelled as S_N and S_S, and some other shell-like faint features which are aligned along an axis of PA$\sim -25^{\circ}$. When shells are well aligned along a certain axis, this axis is always close to the major axis of the galaxy (Prieur 1990), which is out case. Shells can be found in a wide range of radii from the nucleus, from only a few to hundreds of Kpc, such us in the case of NGC 3923 (Prieur 1988). The innest shell detected in 3C 120 is at around 1 arcsec north ($\sim$ 1 kpc) of the nucleus. Shells found close to the nucleus implies that a dissipative process has played an important role in the formation of the shells (Prieur 1990). Therefore, the presence of the detected circumnuclear shells (section §4.1) strongly suggests the idea of considering 3C 120 as a late stage merger.

The arm-like clumpy structures A and B (section §4.1) show kinematics that resembles those of a spiral arm as explained in section §6. However, spiral arms are active star forming regions, and no star formation was detected in either of the continuum-dominated structures. In that case, these structures could be also the remnant of a merging process. Indeed, the regions B, A and the S_s seem to be connected in our residual and color maps (Fig 3C and 4B), and S_s is associated with the E_2 EELR. A kinematics feature (Fig. 11B) is coincident with these structures. Numerical simulations indicate that these kind of structures are found as remnants of merging processes (e.g. Howard et al. 1993; Heyl, Hernquist, & Spergel 1996; Mihos & Hernquist 1996) being difficult to be explained by any other mechanism. Assuming that scenario, the presence of an over density of gas in the south shell may indicate an inflow, where the warmer gas has dropped faster into the inner regions. This picture is in good agreement with the kinematics features at the south shell (E_2 clouds kinematics) and its residuals. The regular velocity in this region suggests that this inflow may occur in a plane outside the galactic disk and close to the line of sight. Although the kinematics of the merger remnants strongly depends on the viewpoint, the velocity and velocity dispersion measured for E_2 is in good agreement with merger simulations (Heyl, Hernquist, & Spergel 1996). Theoretical models indicate that inflows channeling gas from the outer to the nuclear regions may appear in the late stages of a merging process (e.g. Mihos & Hernquist 1996). These inflows have been already observed in different merging galaxies (e.g. Arribas & Colina

2002, 2003). The discussion above suggests that the structures A, B, and the E_2 EELR can be identified with a tidal tail driving material to the central region most probably due to a past merger event in 3C 120. Most of the analyzed continuum dominated structures shows a rather young stellar population, indicating a recent (but not ongoing) star formation rate. This result agrees with the picture of a post-merging event. Similar results have been found in the study of the optical colors of host galaxies AGNs (Jahnke, Kuhlbrodt, & Wisotzki 2004; Sánchez et al. 2004b) .

The poor spatial coverage of the third identified EELR, E_3, prevents us of drawing a clear picture of its origin. In fact, this region corresponds (see section §5.1) to a tail extension of a larger structure already reported in this object (Soubeyran et al. 1989). Although we cannot be conclusive with our current data, the kinematical results most probably indicate that E_3 is associated with an inflow/outflow of gas to/from the circumnuclear region.

It has long been suggested that strong interactions and galaxy mergings may (re-)ignite nuclear activity (e.g. Sanders et al. 1988). Galaxy interactions can produce the loss of momentum required to allow the infall of gas towards the nuclear regions, gas that would feed the AGN. Many authors found that AGN hosts show distorted morphologies, reminiscent of past merging events (e.g. McLeod & Rieke 1994a,b; Bahcall et al. 1997; Sánchez & González-Serrano 2003). They are found in environments with high probability of experiencing interactions (e.g. Sánchez & González-Serrano 2002). And their hosts, mostly early-type galaxies, present anomalous blue colors (e.g. Sánchez et al. 2004a). All together it may indicate that, if not all, at least a family of AGNs is generated by the merging/interaction between galaxies (Canalizo & Stockton 2001). A merging event alone id not enough to generate an AGN. The presence of a massive black-hole in the progenitor galaxy is a basic requerement. Massive black-holes are only found in bulge-dominated massive galaxies, due to the black-hole/bulge mass relation (e.g. Magorrian et al. 1998; Kormendy & Gebhardt 2001). Indeed, recent results (Sánchez et al., in prep.) show that the fraction of AGNs increases in galaxy mergers between two large galaxies or a large with an small galaxy.

Our current results agree with this sceneario. 3C 120 is a bulge dominated galaxy which has, most probably, experienced a merging event with a less massive galaxy. That galaxy was completely disrupted in the merging process, falling in parts which produce, most probably, many of the observed structures (Moles et al. 1988). This may explain the different stellar populations of the structures and the average stellar population in the object (§4.2) as it has been previously reported for other galaxies (Prieur 1990). A subtantial fraction of its gas has been channelled towards the inner regions, following the detected arm-like structure, and concentrating in the E_2 region.

8. Summary

We obtained integral field optical spectroscopy of the Seyfert 1 radio galaxy 3C 120. The homogeneous data, excellent spatial and spectral coverage, and good spatial and spectral resolution make this atlas a useful tool for studying 3C 120 in the optical. These IFS optical data were combined with high resolution HST imaging. The analysis of these data suggests that a Seyfert 1 nucleus at the center, an early type galaxy, and several structures formed as a consequence of a merging process in the past history constitute the radio galaxy 3 120. At least one of these structures is identified with an inflow, which is feeding the central engine. A radio-jet is escaping from the center, perturbing the gas on its path.

The main results from the analysis of this dataset were the following:

1. Several continuum-dominated structures were detected in 3C 120, which do not follow the mean distribution (bulge dominated) of the stellar component. Some of these structures were shells in the central Kpc of the object, which may indicate a past merging process. The colors of the different components were not compatible with a single stellar population in this galaxy.

2. Three emission line structures were identified (E_1, E_2 and E_3) which were not associated with the general behavior of the galaxy. These gaseous structures presented a high level of ionization. The origin of structure E_1 was the interaction between the intergalactic medium and the radio-jet emerging from the nucleus.

2. The spectra of the nucleus and the host galaxy were decoupled, obtaining a data cube of residuals. From that residual data cube, we extracted and analyzed the spectra of the different structures in 3C 120.

3. The velocity field indicated a rotational component plus several kinematical perturbations associated with the identified emission structures.

4. The continuum-dominated structures A, B, the S_s shell and the EELR E_2 seem to be physically associated, belonging to the inner-most part of a tidal-tail, remanent of a past merging event. This tail has channeled gas into the inner regions, in an inflow, that has generated E_2.

The 4.2-m William Herschel Telescope is operated by the Isaac Newton Group at the Observatorio de Roque de los Muchachos of the Instituto de Astrofísica de Canarias. We thank all the staff at the Observatory for their kind support. This project is part of the Euro3D RTN on IFS, funded by the EC under contract No. HPRN-CT-2002-00305. This

project has used images obtained from the HST archive, using the ESO archiving facilities. We would like to thank Dr.Walker that has kindly provided us with the radio maps of 3C 120.

A. Atlas of spectra

In this appendix we present the spatial distribution of the brightest emission line profiles as spectra diagrams. These diagrams represent line profiles in a short wavelength range of the individual spectra at each point (fiber). The spectra at each location are autoscaled to show the profile shape (lines nearer to the optical nucleus are brighter than those farther out). Figure 13 and 14 show the spectra diagrams corresponding to Hβ+[OIII]$\lambda\lambda$4959, 5007, and Hα+[NII]$\lambda\lambda$6548, 6584+[SII]$\lambda\lambda$6716, 6730, respectively. A considerable blending of the emission lines with the wings of the broad component of the Balmer lines can be clearly appreciated in these diagrams.

B. Decoupling the spectra of different components using IFS

A new technique to decouple the spectra of different components in an object has been developed, based on well known techniques applied in the decoupling of different components in images. Two different methods have been developed. A first one is based on a 2D modeling of the objects using object templates, while the second one is based on an isophotal analysis of 2D images. We explain here how both methods have been extended to the analysis of IFS datacubes, and the advantages of each one.

B.1. 3D modeling

IFS combines the characteristics of imaging and spectroscopy. In general terms, IFS data consist of a series of spectra obtained at a discrete number of positions in the sky. In the case of INTEGRAL data in the SB2 configuration, they consist of the 209 spectra obtained in the same number of positions in the sky. Newer instruments, like PMAS (Roth et al. 2000) or VIMOS (LeFevre et al. 2003), sample the sky in a continuous way, by coupling the fibres to lens-arrays. In these latter cases a IFS datacube can be understood as a stack of narrow-band images. More generally, at each wavelength we have a 2D discrete distribution of fluxes, that can be transformed to a regular grid distribution by an interpolation routine.

It is a quite common situation that an observed object is the combination of different components: e.g., an QSO lens, a crowded-field of stars and an AGN+host system. Different techniques have been developed to decouple the different components of an image, and to derive their photometry. A wide extended technique is to fit the images with a 2D model, including a template for each different component. This technique is implemented in GALFIT (Peng et al. 2002), a program for modeling multi-components in images. This

program has been used in the decoupling of nuclear and host components (Sánchez et al. 2004b) and the decoupling of different components in a QSO lens (Wisotzki et al. 2004). GALFIT fits the images with a multi-component model, producing a template image and a residual image. This residual image can be used to detect substructures in 2D images.

A natural extension of the 2D modeling technique to IFS is to split the datacube in a set of narrow-band images of the width of the spectral pixel (the so-called monochromatic images), and treat them as individual images. This technique has been used successfully for the deblending of QSO lenses with IFS (Wisotzki et al. 2003). In the particular case of our INTEGRAL data, we first transformed the discrete set of spectra in a regular grid datacube using an interpolation routine implemented in E3D (Sánchez 2004). The final datacube has a $0\farcs3 \times 0\farcs3$ pixel size, i.e., 1/3th of the original diameter of the fibers.

The 2D image modeling of the nucleus and the host for each monochromatic image was performed using GALFIT. The 2D model comprises a narrow Gaussian function (to model the nucleus) and a de Vaucouleurs law (to model the galaxy), both convolved with a PSF. The PSF at each wavelength was obtained from a calibration star datacube, observed just before the object. In a first attempt all the parameters of the model were fitted: the intensities of the nucleus and the host, the centroid of the object, the effective radius, the position angle and the ellipticity of the host galaxy. As already noticed by Wisotzki et al. (2003), this first modeling does not produce acceptable results. The large number of parameters, the degeneracy between some of them (e.g., the total intensity and the scale-length), and the limited sampling of our data impose limitations to the quality of the recovered spectra.

However, Wisotzki et al. (2003) demonstrated that it is possible to increase the quality of the modeling imposing certain conditions in the structural parameters. The centroid of the object varies through the wavelengths due to differential atmospheric refraction (DAR) (Filippenko 1982). Therefore, whenever there is a clear peak in the object (like in our case) the centroid should vary smoothly with the wavelength. Figure 15 shows the centroid coordinates as a function of the wavelength resulting from the 3D modeling. Despite of the fluctuations, there is a clear trend. The solid-lines show the result of a fitting a polynomial function of order 5. In a second run of the 3D modeling we imposed the centroid to be fixed to the result from this polynomial fitting. Similar conditions can be imposed for the ellipticity, effective radius and position angle of the host galaxy. By forcing the structural parameters to vary smoothly with the wavelength and fixing them in the 3D modeling process the number of parameters is reduced to the intensity of the different components. Thus the accuracy of the modeling is increased (Wisotzki et al. 2003, 2004).

The number of parameters can be reduced too if we derive the structural parameters from an external source of information. As we explained above we have good quality HST

images of the object in different bands, that have been already analyzed using GALFIT (§4.1). We fixed the structural parameters (effective radius, ellipticity and position angle) in our second 3D modeling of the values derived by the 2D modeling of the HST images (Table 2). The centroids were fixed to the values derived using the polynomial function shown in Fig. 15. Figure 16 illustrates the process. The top-left panel shows the decoupled spectra of the nucleus and the host derived from the 3D modeling when all the parameters are fitted freely. The spectra derived from the first run are noisy and can only be considered as a very rough approximation. The top-right panel shows the spectra once fixed the centroids to the result of the polynomial function fitting shown in Fig. 15. There is a clear increase of the quality of the derived spectra. The bottom-left panel shows the spectra when, in addition to the centroids, the structural parameters of the host galaxy (ellipticity, position angle and effective radius) are fix to the result from a polynomial function fitting similar to the one used for the centroids. This is the best possible result if we only had the information from the IFS. The bottom-right panel shows the final result, obtained when the structural parameters are fixed to the values derived from the 2D modeling of the HST images. The derived spectra are remarkable similar to those of the previous case. However, in the previous case it is possible to identify some *fake* absorption features in the spectrum of the nucleus coincident with the narrow emission lines (e.g., [OIII]λ5007). We cross-checked the accuracy of the final decoupled spectra by comparing the fluxes derived with that obtained by the 2D modeling of the HST images. Both fluxes agree within $\sim$20%.

As we explained above GALFIT provides us with a residual image at each wavelength once subtracted the 2D model from each monochromatic image. We stored and stacked those residual images to create a residual datacube. The residual datacube is used (1) to cross-check the accuracy of the fitting, i.e., no evident fake residuals are found, and (2) to study the substructures in the object. Figure 17, left panel, shows a narrow-band image centred in the continuum adjacent to the [OIII] emission line (5204-5246Å) from the residual datacube (contour-plots), together with the residual image obtained by a 2D modeling of the HST F555W-band image (grayscale). A simple comparison of both images shows that the residuals are remarkable similar outside $\sim$2″ from the nucleus. However, there is a ring structure at $\sim$1.″5, $\sim$100 fainter than the nucleus, expecially bright in the S_S of the nucleus. This structure coincides somehow with the south-east shell. However it is worrisome that it is fainter in the north-west, where the S_N shell is brighter. Taking into account the original size of the fibers ($\sim$0.″9) and our limited determination of the PSF, we think that this ring substructure is an artifact of the 2D modeling. Although it limits the use of the residual datacube to study the properties of the substructures, it does not significantly affect the accuracy of the decoupled spectra.

B.2. 3D surface brightness analysis

We developed a second method to create a 3D template of the object that would not depend on the PSF determination and without assuming any certain law to describe the intensity profile. This method is an extension of the isophotal surface brightness analysis technique (Jedrzejewski 1987). It looks for the ellipse parameters that better represent the isophotal shape by a Fourier analysis of the surface brightness at a certain radius as a function of the eccentric anomaly. The output is a surface brightness profile of the object (i.e., the radial distribution of the intensity), and the radial distributions of the centroid, position angle and ellipticity (understanding radius as semi-major axis of the ellipse). A template of the object is created using these output parameters. Then, a residual of the image is obtained by subtracting this template from the original image. This technique has been extensively used for the detection of substructures in galaxies for decades (e.g. Pérez-Fournon et al. 1986; Hjorth et al. 1995).

We extended this method to analyze substructures in IFS data. For each monochromatic image we performed an isophotal surface brightness analysis using our own coded routines. The average centroids, ellipticities, position angles, and the integrated fluxes obtained from this analysis are stored for each wavelength. The residual images obtained are combined in a residual datacube. Like in the previous method the quality of the model template can be increased assuming that the structural parameters change smoothly with the wavelength. The structural parameters for each wavelength were fixed to the values derived by a polynomial function fitting. In the case of an isophotal analysis, once fixed the structural parameters, the derived model for each monochromatic image is just estimated obtaining the average flux at a certain radius along the eccentric anomaly. I.e., it is not a fit anymore, but just a direct measurement.

Figure 18 illustrates the results of this process. It shows, in both panels, the integrated spectrum of 3C 120 over the field-of-view of INTEGRAL (black line), together with the recovered spectrum from the 3D template (orange line), and the integrated spectrum of the residuals. The left panel shows the result from the first iteration where all the structural parameters are derived by the described method. In general terms the spectrum of the model matches well the original spectrum, despite some wavelengths where the program is unable to derive the correct parameters. The right panel shows the result from the second iteration with all the structural parameters fixed, as described above. In this case the agreement between the recovered and the original spectrum is remarkable good, with no flux deviation higher than a few percent at any wavelength.

As expected this method produces a better quality residual datacube than the 3D modeling. The basic reason is that we reduced the number of assumptions about the shape of

the object and we transformed a fit to a direct measurement. Figure 17, right panel, shows a similar narrow-band image of the continuum adjacent to [OIII] from the residual datacube than the one presented in the left panel, but obtained with the 3D surface brightness analysis. The grayscale shows once more the residual from the 2D modeling of the F555W-band image. The residuals from the narrow-band image and the HST data match better than that of the 2D modeling. No trace of the ring structure is present, which reinforce our idea that it is an spurious result due to a limited sampling and inaccuracies in the PSF determination.

The two developed techniques to decoupling spectra of different components from IFS data give successful results. The first method could be useful to deblend spectra, such in the case of spectra from different components. The second procedure is more suitable to study the residual structures once the spectrum of the main component is subtracted.

REFERENCES

Arribas, S., Carter, D., Cavaller, L., del Burgo, C., Edwards, R., Fuentes, F. J., Garcia, A. A., Herreros, J. M., Jones, L. R., Mediavilla, E., Pi, M., Pollacco, D., Rasilla, J. L., Rees, P. C., & Sosa, N. A. 1998, in Proc. SPIE Vol. 3355, p. 821-827, Optical Astronomical Instrumentation, Sandro D'Odorico; Ed., 821–827

Arribas, S. & Colina, L. 2002, ApJ, 573, 576

—. 2003, ApJ, 591, 791

Arribas, S., Mediavilla, E., García-Lorenzo, B., del Burgo, C., & Fuensalida, J. J. 1999, A&AS, 136, 189

Axon, D. J., Pedlar, A., Unger, S. W., Meurs, E. J. A., & Whittle, D. M. 1989, Nature, 341, 631

Bahcall, J. N., Kirhakos, S., Saxe, D. H., & Schneider, D. P. 1997, ApJ, 479, 642

Baldwin, J. A., Carswell, R. F., Wampler, E. J., Boksenberg, A., Smith, H. E., & Burbidge, E. M. 1980, ApJ, 236, 388

Bingham, R. G., Gellatly, D. W., Jenkins, C. R., & Worswick, S. P. 1994, in Proc. SPIE Vol. 2198, p. 56-64, Instrumentation in Astronomy VIII, David L. Crawford; Eric R. Craine; Eds., 56–64

Binney, J. & Merrifield, M. 1998, Galactic astronomy (Galactic astronomy / James Binney and Michael Merrifield. Princeton, NJ : Princeton University Press, 1998. (Princeton series in astrophysics) QB857 .B522 1998 ($35.00))

Bruzual, G. & Charlot, S. 2003, MNRAS, 344, 1000

Cairós, L. M., Caon, N., García-Lorenzo, B., Vílchez, J. M., & Muñoz-Tuñón, C. 2002, ApJ, 577, 164

Canalizo, G. & Stockton, A. 2001, ApJ, 555, 719

Chabrier, G. 2003, PASP, 115, 763

de Vaucouleurs, G. 1948, Ann. Astrophys., 11, 247

Filippenko, A. V. 1982, PASP, 94, 715

Fitzpatrick, E. L. 1999, PASP, 111, 63

Fraix-Burnet, D., Golombek, D., & Macchetto, F. D. 1991, AJ, 102, 562

Fukugita, M., Shimasaku, K., & Ichikawa, T. 1995, PASP, 107, 945

García-Lorenzo, B., Acosta-Pulido, J. A., & Megias-Fernández, E. 2002, in ASP Conf. Ser. 282: Galaxies: the Third Dimension, 501–+

García-Lorenzo, B., Arribas, S., & Mediavilla, E. 2001, A&A, 378, 787

González-García, C., & Balcells, M. 2003, MNRAS, submitted

Hansen, L., Jorgensen, H. E., & Norgaard-Nielsen, H. U. 1987, A&AS, 71, 465

Hernquist, L. & Spergel, D. N. 1992, ApJ, 399, L117

Heyl, J. S., Hernquist, L., & Spergel, D. N. 1996, ApJ, 463, 69

Hjorth, J., Vestergaard, M., Sorensen, A. N., & Grundahl, F. 1995, ApJ, 452, L17+

Howard, S., Keel, W. C., Byrd, G., & Burkey, J. 1993, ApJ, 417, 502

Hua, C. T. 1988, A&A, 199, 105

Jahnke, K. 2002, PhD thesis, University of Hamburg, http://www.sub.uni-hamburg.de/disse/726/dissertation.pdf

Jahnke, K., Kuhlbrodt, B., & Wisotzki, L. 2004, MNRAS, 352, 399

Jahnke, K., Wisotzki, L., Sánchez, S., Christensen, L., Becker, T., Kelz, A., & Roth, M. 2004, AN

Jedrzejewski, R. I. 1987, MNRAS, 226, 747

Knapen, J. H., Whyte, L. F., de Blok, W. J. G., & van der Hulst, J. M. 2004, A&A, 423, 481

Kormendy, J. & Gebhardt, K. 2001, in AIP Conf. Proc. 586: 20th Texas Symposium on relativistic astrophysics, 363

LeFevre, O., Saisse, M., Mancini, D., Brau-Nogue, S., Caputi, O., Castinel, L., D'Odorico, S., Garilli, B., Kissler-Patig, M., Lucuix, C., Mancini, G., Pauget, A., Sciarretta, G., Scodeggio, M., Tresse, L., & Vettolani, G. 2003, in Instrument Design and Performance for Optical/Infrared Ground-based Telescopes. Edited by Iye, Masanori; Moorwood, Alan F. M. Proceedings of the SPIE, Volume 4841, pp. 1670-1681 (2003)., 1670–1681

Lilly, S. J. & Longair, M. S. 1984, MNRAS, 211, 833

Magorrian, J., Tremaine, S., Richstone, D., Bender, R., Bower, G., Dressler, A., Faber, S. M., Gebhardt, K., Green, R., Grillmair, C., Kormendy, J., & Lauer, T. 1998, AJ, 115, 2285

Malin, D. F. & Carter, D. 1983, ApJ, 274, 534

McCarthy, P. J., van Breugel, W., Spinrad, H., & Djorgovski, S. 1987, ApJ, 321, L29

McLeod, K. K. & Rieke, G. H. 1994a, ApJ, 420, 58

—. 1994b, ApJ, 431, 137

Mediavilla, E., Arribas, S., del Burgo, C., Oscoz, A., Serra-Ricart, M., Alcalde, D., Falco, E. E., Goicoechea, L. J., Garcia-Lorenzo, B., & Buitrago, J. 1998, ApJ, 503, L27+

Mihalas, D. & Binney, J. 1981, Galactic astronomy: Structure and kinematics /2nd edition/ (San Francisco, CA, W. H. Freeman and Co., 1981. 608 p.)

Mihos, J. C. & Hernquist, L. 1996, ApJ, 464, 641

Moles, M., del Olmo, A., Masegosa, J., & Perea, J. D. 1988, A&A, 197, 1

Motta, V., Mediavilla, E., Muñoz, J. A., Falco, E., Kochanek, C. S., Arribas, S., García-Lorenzo, B., Oscoz, A., & Serra-Ricart, M. 2002, ApJ, 574, 719

Ogle, P. M., Davis, S. W., Antonucci, R. R. J., Colbert, J. W., Malkan, M. A., Page, M. J., Sassen, T. P., & Tornikoski, M. T. 2004, ApJ

Osterbrock, D. E. 1989, Astrophysics of gaseous nebulae and active galactic nuclei (University Science Books, 1989, 422 p.)

Pérez-Fournon, I., Colina, L., Biermann, P., & Marcaide, J. M. 1986, in IAU Symp. 119: Quasars, 127

Peng, C. Y., Ho, L. C., Impey, C. D., & Rix, H. 2002, AJ, 124, 266

Phillips, M. M. & Osterbrock, D. E. 1975, PASP, 87, 949

Prieur, J. L. 1990, in Wielen R., ed., Dynamics and Interactions of Galaxies, Springer-Verlag, Berlin, 72

Prieur, J. L. 1988, ApJ, 326, 596

Readhead, A. C. S., Pearson, T. J., Cohen, M. H., Ewing, M. S., & Moffet, A. T. 1979, ApJ, 231, 299

Roth, M. M., Bauer, S., Dionies, F., Fechner, T., Hahn, T., Kelz, A., Paschke, J., Popow, E., Schmoll, J., Wolter, D., Laux, U., & Altmann, W. 2000, in Proc. SPIE Vol. 4008, p. 277-288, Optical and IR Telescope Instrumentation and Detectors, Masanori Iye; Alan F. Moorwood; Eds., 277–288

Sánchez, S. F. & González-Serrano, J. I. 2002, A&A, 396, 773

Sánchez, S. 2004, AN, 325, 167

Sánchez, S. F., García-Lorenzo, B., Mediavilla, E., González-Serrano, J., & Christensen, L. 2004a, ApJ, (accepted) (astro-ph/0407128)

Sánchez, S. F. & González-Serrano, J. I. 2003, A&A, 406, 435

Sanchez, S. F., Jahnke, K., Wisotzki, L., & et al. 2004b, ApJ, 614, 586

Sanders, D. B., Soifer, B. T., Elias, J. H., Neugebauer, G., & Matthews, K. 1988, ApJ, 328, L35

Sargent, W. L. W. 1967, PASP, 79, 369

Schweizer, F., & Seitzer, P. 1988, ApJ, 328, 88

Sèrsic, J. L. 1968, in Atlas de Galaxes Australes; Vol. Book; Page 1

Soubeyran, A., Wlerick, G., Bijaoui, A., Lelievre, G., Bouchet, P., Horville, D., Renard, L., & Servan, B. 1989, A&A, 222, 27

Tadhunter, C. N., Dickson, R. C., & Shaw, M. A. 1996, MNRAS, 281, 591

Tody, D. 1986, in Instrumentation in astronomy VI; Proceedings of the Meeting, Tucson, AZ, Mar. 4-8, 1986. Part 2 (A87-36376 15-35). Bellingham, WA, Society of Photo-Optical Instrumentation Engineers, 1986, p. 733., 733–+

Veilleux, S. & Osterbrock, D. E. 1987, ApJS, 63, 295

Walker, R. C. 1997, ApJ, 488, 675

Walker, R. C., Benson, J. M., & Unwin, S. C. 1987, ApJ, 316, 546

Walker, R. C., Walker, M. A., & Benson, J. M. 1988, ApJ, 335, 668

Williams, R. E., & Christiansen, W. A. 1985, ApJ, 291, 80

Wisotzki, L., Becker, T., Christensen, L., Helms, A., Jahnke, K., Kelz, A., Roth, M. M., & Sanchez, S. F. 2003, A&A, 408, 455

Wisotzki, L., Schechter, P. L., Chen, H.-W., Richstone, D., Jahnke, K., Sánchez, S. F., & Reimers, D. 2004, A&A, 419, L31

Zwicky, F. & Zwicky, M. A. 1971, Catalogue of selected compact galaxies and of post-eruptive galaxies (Guemligen: Zwicky, —c1971)

Zirbel, E.L. & Baum, S.A. 1998, ApJS, 114, 177

This preprint was prepared with the AAS LaTeX macros v5.2.

Table 1: Summary of properties of the HST images

Band	Exp.Time (s)	3σ lim. mag (mag/arcsec^2)	mag	mag NED
F555W (V)	2040	25.3	14.94	14.7
F547M (V')	2300	25.1	14.35	—-
F675W (R)	2250	25.3	13.74	13.9
F814W (I)	2236	24.9	(1)	12.9

(1) Peak saturated.

Table 2: Summary of the result from the 2D modeling

Band	n	m_{nuc}	m_{host}	r_e	a/b	PA(^{o})
F555W	4.7	16.1	15.4	1.9 kpc	0.87	−16.8
F547M	4.5	16.9	14.5	2.9 kpc	0.86	−18.6
F675W	6.7	16.1	13.9	2.8 kpc	0.73	−19.1
F814W	—	—-	13.2	——-	0.94	−18.5

Table 3: Properties of the emission lines detected in the nucleus and host galaxy of 3C 120

Name	Line	λ^1	σ_λ	Flux^2	
Nucleus	Hδ^3	4250.33	24.12	61.25	260.78
	HδBL1	4249.15	24.12	319.60	583.19
	HδBL2	4254.50	24.12	1754.62	516.10
	Hγ	4498.42	24.12	35.08	268.68
	HγBL1	4497.24	24.12	885.98	539.97
	HγBL2	4502.58	24.12	790.73	422.00
	[OIII]λ4363	4521.98	24.12	60.99	119.60
	HeIIλ4686BL1	4846.66	24.12	192.56	100.54
	HeIIλ4686BL2	4876.41	24.12	270.39	141.18
	Hβ	5024.82	0.19	75.54	479.99
	HβBL1	5028.23	1.76	1473.31	754.88
	HβBL2	5058.85	53.77	1676.73	788.82
	[OIII]λ4959	5125.77	0.19	163.17	35.06
	[OIII]λ5007	5175.36	0.19	489.58	105.20
	HeIλ5876BL1	6075.86	11.62	332.05	112.13
	HeIλ5876BL2	6105.86	11.62	465.42	157.05
	[OI]λ6300.3	6518.52	40.42	20.34	33.63
	[OI]λ6363.8	6584.19	40.42	30.34	34.81
	[NII]λ6548	6784.48	2.08	9.46	57.34
	Hα	6799.71	2.08	232.62	513.60
	HαBL1	6782.94	0.58	3570.51	574.07
	HαBL2	6797.59	1.15	5985.15	446.94
	[NII]λ6583	6821.21	2.08	28.40	172.13
HOST	[OII]λ3727	3867.81	10.22	477.51	60.96
	[NeIII]λ3869	4010.57	16.32	332.54	48.24
	[NeIII]λ3967	4117.10	16.32	179.77	34.32
	[SII]λ4072	4223.39	122.12	110.88	37.32
	Hγ	4494.84	389.92	54.84	28.56
	[OIII]λ4364	4518.40	389.92	56.88	28.32
	HeIIλ4686	4851.17	143.31	101.76	33.48
	Hβ	5030.04	0.82	218.05	39.72
	[OIII]λ4959	5131.00	0.82	1164.08	161.37
	[OIII]λ5007	5180.58	0.82	3495.62	484.59
	HeIλ5876	6072.99	23.27	45.60	47.40
	[OI]λ6300	6514.63	194.46	122.40	60.48
	[OI]λ6364	6580.30	194.46	58.08	55.20
	[NII]λ6548	6771.69	2.31	259.45	46.92
	Hα	6786.91	2.31	2097.63	255.97
	[NII]λ6583	6808.41	2.31	778.37	140.77
	[SII]λ6716	6946.13	32.68	368.18	96.00
	[SII]λ6731	6961.00	32.68	248.29	89.52
	ArIII	7377.62	291.60	108.48	69.00

(1) wavelength in Å, (2) flux in 10^{-16} erg s^{-1} cm^{-2}units, (3) the narrow-emission lines had a velocity dispersion of ∼700 km s^{-1}, while the broad-emission lines have to component, BL1 and BL2, with a velocity dispersion of ∼2188 km s^{-1}and ∼8706 km s^{-1}, respectively.

Table 4: Properties of the emission lines detected in the EELRs of 3C 120

Name	Line	λ^1	σ_λ	Flux^2	
E_1	[OII]λ3727	3868.81	8.63	1.45	0.38
	[NeIII]	4015.92	8.63	0.13	0.02
	[NeIII]	4117.45	8.63	0.68	0.09
	Hβ	5032.50	3.74	2.11	0.17
	[OIII]λ4959	5133.57	3.74	9.52	1.21
	[OIII]λ5007	5183.20	3.74	28.55	3.64
	[NII]λ6548	6775.53	8.62	1.53	0.13
	Hα	6790.75	8.62	16.32	1.39
	[NII]λ6583	6812.25	8.62	4.62	0.40
	[SII]λ6716	6948.04	58.25	2.63	0.24
	[SII]λ6731	6962.91	58.25	2.06	0.21
E_2	[OII]λ3727	3864.80	10.25	7.08	0.55
	[NeIII]	4012.37	13.09	4.29	0.35
	[NeIII]	4111.74	26.17	2.53	0.20
	[SII]	4217.03	82.77	0.56	0.06
	Hδ	4247.03	10.82	1.02	0.11
	Hγ	4493.72	10.82	2.48	0.32
	HeIIλ4686	4850.62	40.48	2.20	0.17
	Hβ	5028.49	0.81	4.95	0.39
	[OIII]λ4959	5129.44	0.81	25.27	3.06
	[OIII]λ5007	5179.03	0.81	75.82	9.18
	HeIλ5876	6077.20	50.43	0.80	0.12
	[OI]λ6300.3	6513.68	40.26	1.63	0.20
	[OI]λ6363.8	6572.96	294.61	0.24	0.04
	[NII]λ6548.1	6770.28	3.38	2.77	0.23
	Hα	6785.51	3.38	25.40	2.04
	[NII]λ6583.6	6807.01	3.38	8.33	0.68
	[SII]λ6716	6946.47	16.71	5.89	0.50
	[SII]λ6731	6961.35	16.71	2.96	0.29
	ArIII	7378.28	51.65	1.48	0.12
E_3	[OII]λ3227	3866.04	14.72	4.54	0.87
	[NeIII]λ3927	4013.15	14.72	2.39	0.28
	Hβ	5032.51	39.54	2.10	0.21
	[OIII]λ4959	5131.26	2.71	11.06	1.53
	[OIII]λ5007	5180.84	2.71	33.21	4.58
	[NII]λ6548	6771.15	6.12	0.41	0.01
	Hα	6786.37	6.12	12.74	1.71
	[NII]λ6584	6807.87	6.12	1.23	0.04
	[SII]λ6716	6946.55	22.92	13.97	1.56
	[SII]λ6731	6961.42	22.92	6.70	0.75

(1) wavelength in Å, (2) flux in 10^{-16} erg s^{-1} cm^{-2}units.

Table 5: Properties of the gaseous emission of the different components in 3C 120

Name	[OIII]λ5007/Hβ [1]	[NII]λ6583/Hα [1]	Hα/Hβ	A_V mags	[SII]λ6716/[SII]λ6731	n_e cm^{-3}	T$_{eff}$ (K)
E$_1$	1.13	-0.54	7.7	3.2	1.3	$\sim$160	—
E$_2$	1.18	-0.48	5.1	1.9	2.0	$\sim$1	—
E$_3$	1.20	-1.02	6.1	2.4	2.0	$\sim$1	—
Nucleus[2]	0.81	-0.91	3.1	–	–	–	2.3×10^5
Host	1.21	-0.43	9.8	4.0	1.5	$\sim$10	1.4×10^4

(1) In logarithms. (2) Narrow emission lines

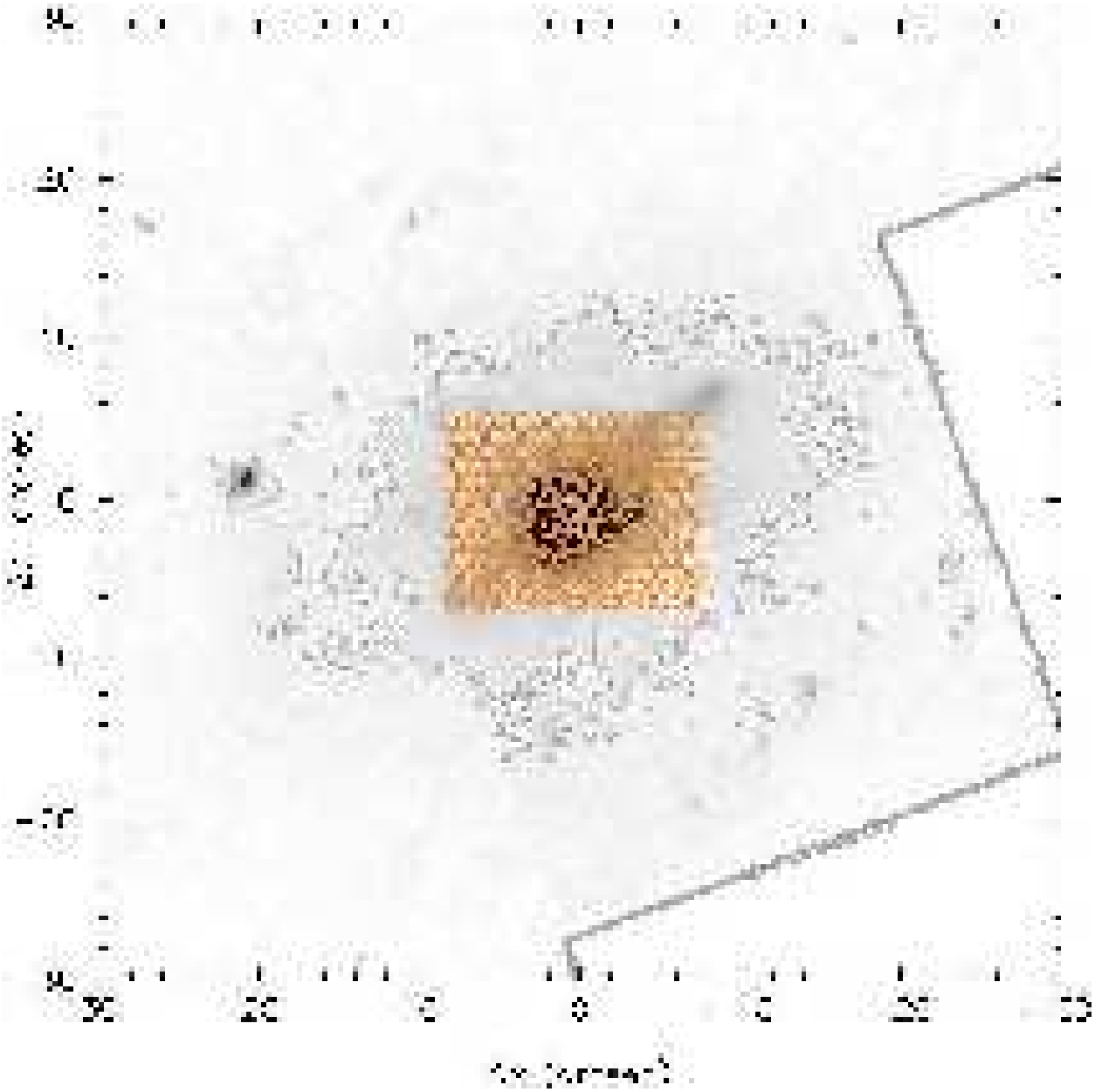

Figure 1: F555W-band image of 3C 120 taken with the WFPC at the HST. The spatial distribution of the science fibers at the focal plane of the 4.2m WHT has been overlaid. North and East are up and left, respectively as usual. The orientation is the same in all figures in this paper.

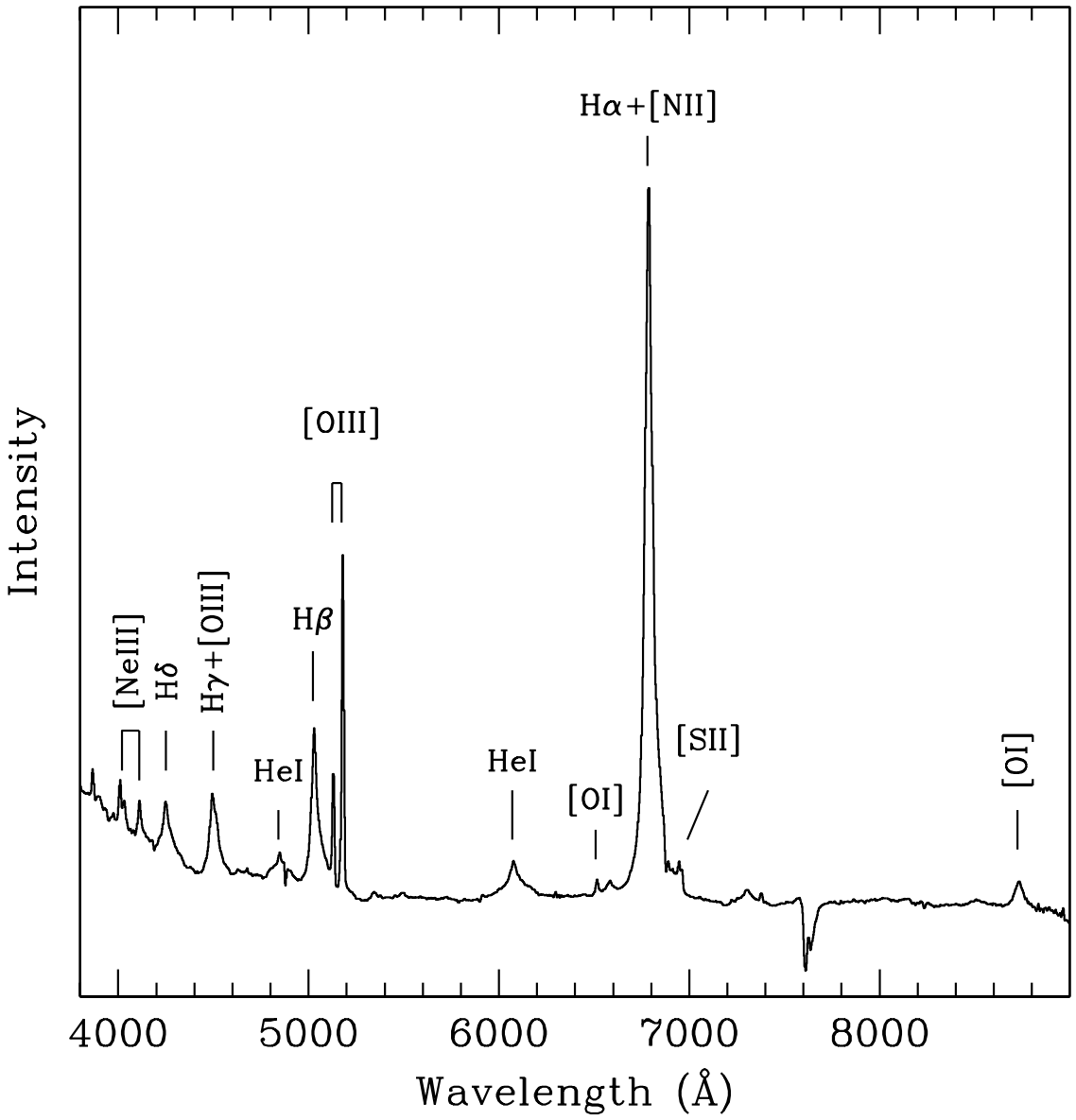

Figure 2: Nuclear spectrum in the full spectral range. This spectrum corresponds to a hexagonal aperture of 1.″6 in radius centred on the optical nucleus.

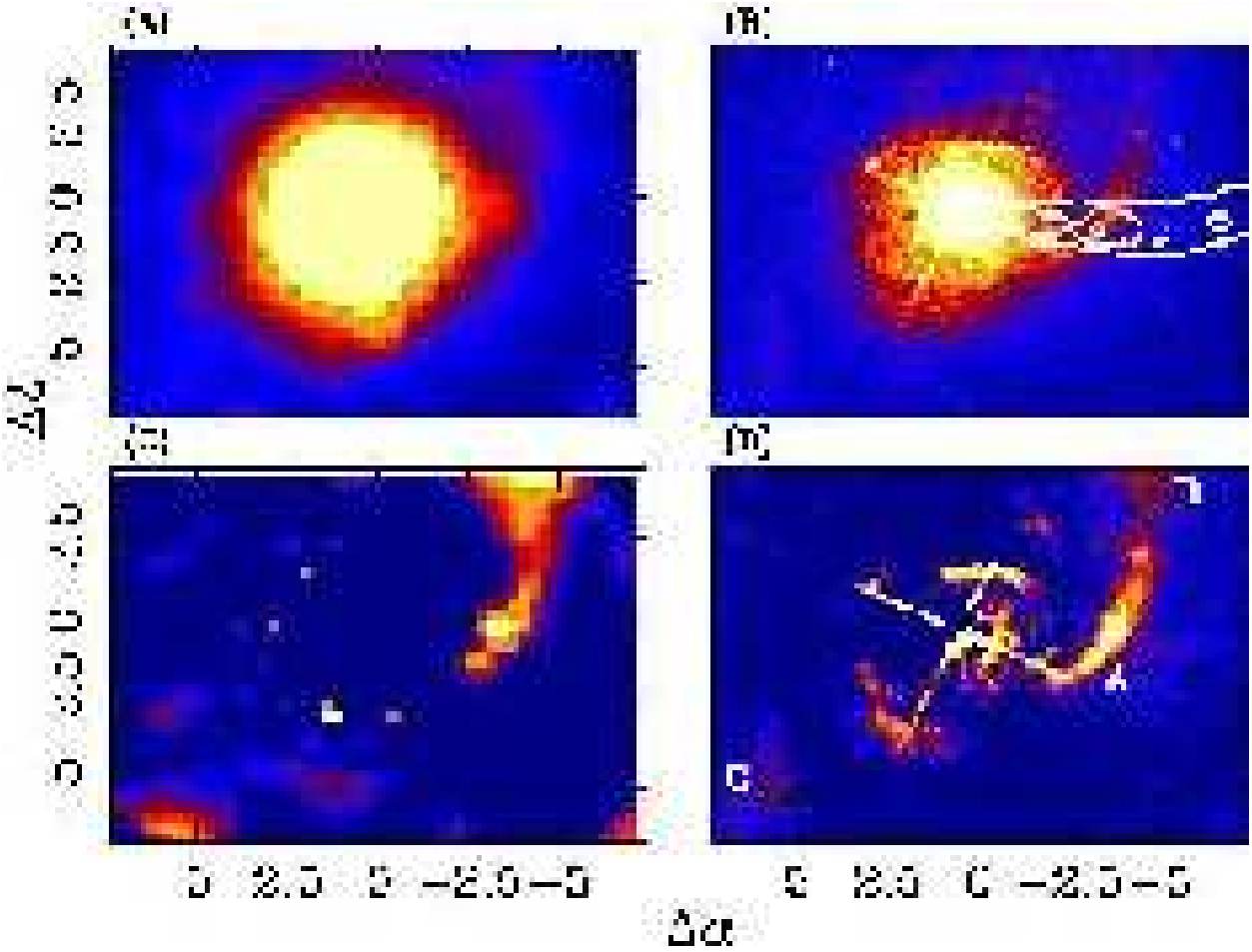

Figure 3: (A) Two-dimensional distribution of the continuum emission of 3C 120 derived from the IFS data by integrating the signal in the spectral range 5100-6100 Å, similar to that range covered by the V-band filter. (B) F555W-band image of the same central region of 3C 120 obtained with the HST/PC (0.″046/pixel). Different continuum dominated structures already detected from ground base observations are labeled using the nomenclature from Soubeyran et al. (1989). The contour-plot shows the radio map at 4885 MHz Walker (1997). (C) V-band residual image, once subtracted the galaxy template derived by a 2D modeling from the V-band image shown in panel (A). (D) F555W-band residual image derived by subtracting a galaxy template obtained by a 2D modeling from the F555W-band image shown in panel (B).

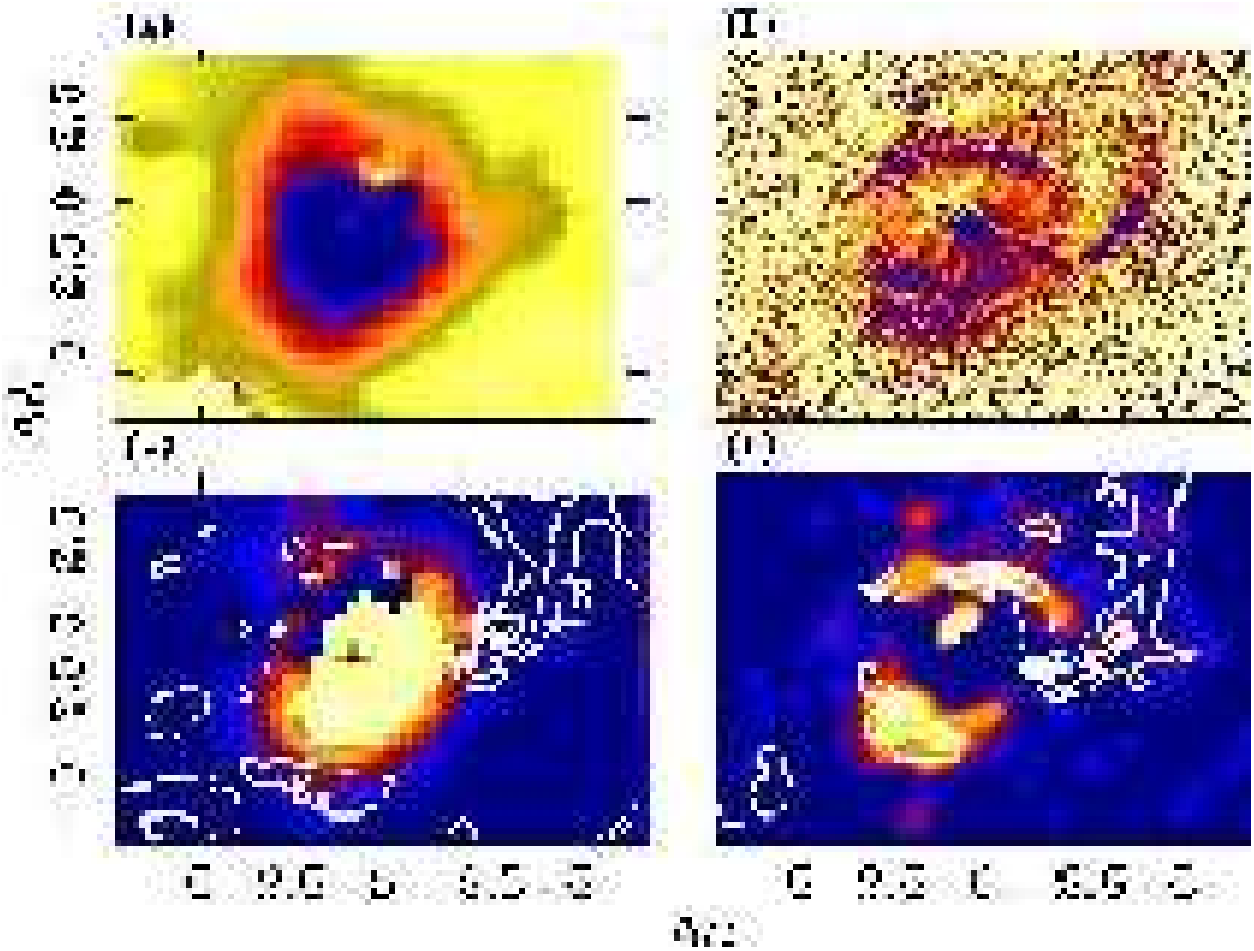

Figure 4: (A) The $V - I$ color image derived from the V and I maps recovered from the IFS data. (B) The $V - I$ color image obtained from the F555W and F675W-band HST images. The image has been smoothed with a 3×3 pixel median kernel. (C) The residual V map (close similar to an ionized gas map) derived subtracting a continuum recovered from the IFS data (5600-5700 Å) avoiding the contribution of any bright emission line and scaled. (D) The residual image obtained by the subtraction of the F547M-band image from the F555W-band image, once scaled by the differences of the photometric zero-points. The contour-plot corresponds to the F555W-band residual image shown in figure 3D. Labels indicate the previously detected EELRs (Soubeyran et al. 1989; Sánchez et al. 2004a).

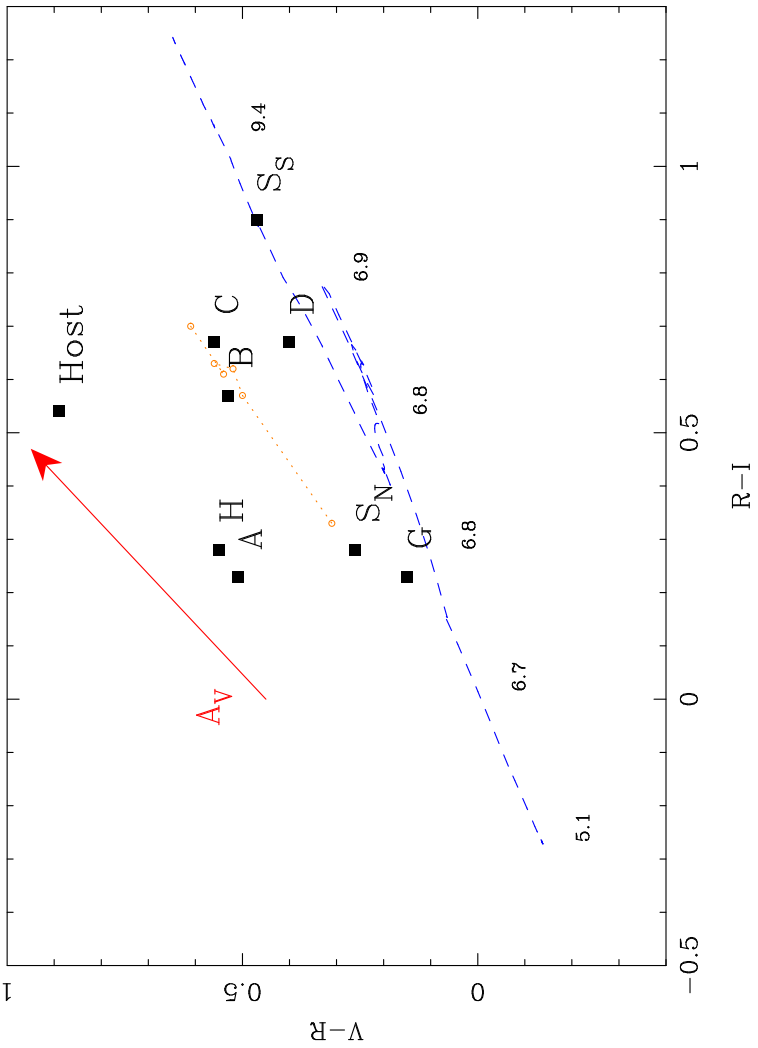

Figure 5: $V - R$ colors as a function of the $R - I$ colors of the host galaxy and the different structures found in 3C 120. The discontinuous line shows the location of a single stellar population model at different ages Bruzual & Charlot (2003). The values indicate the logarithm of the age in Gyrs. The dotted line shows the average colors of different galaxy types (E, Sab, Sbc, Scd and Irr), obtained from Fukugita et al. (1995). The arrow shows the effect of dust in the colors for an absorption of $A_V \sim$1.5 mags. Errors of the individual colors are 0.1 and 0.26 mag in V-R and R-I, respectively.

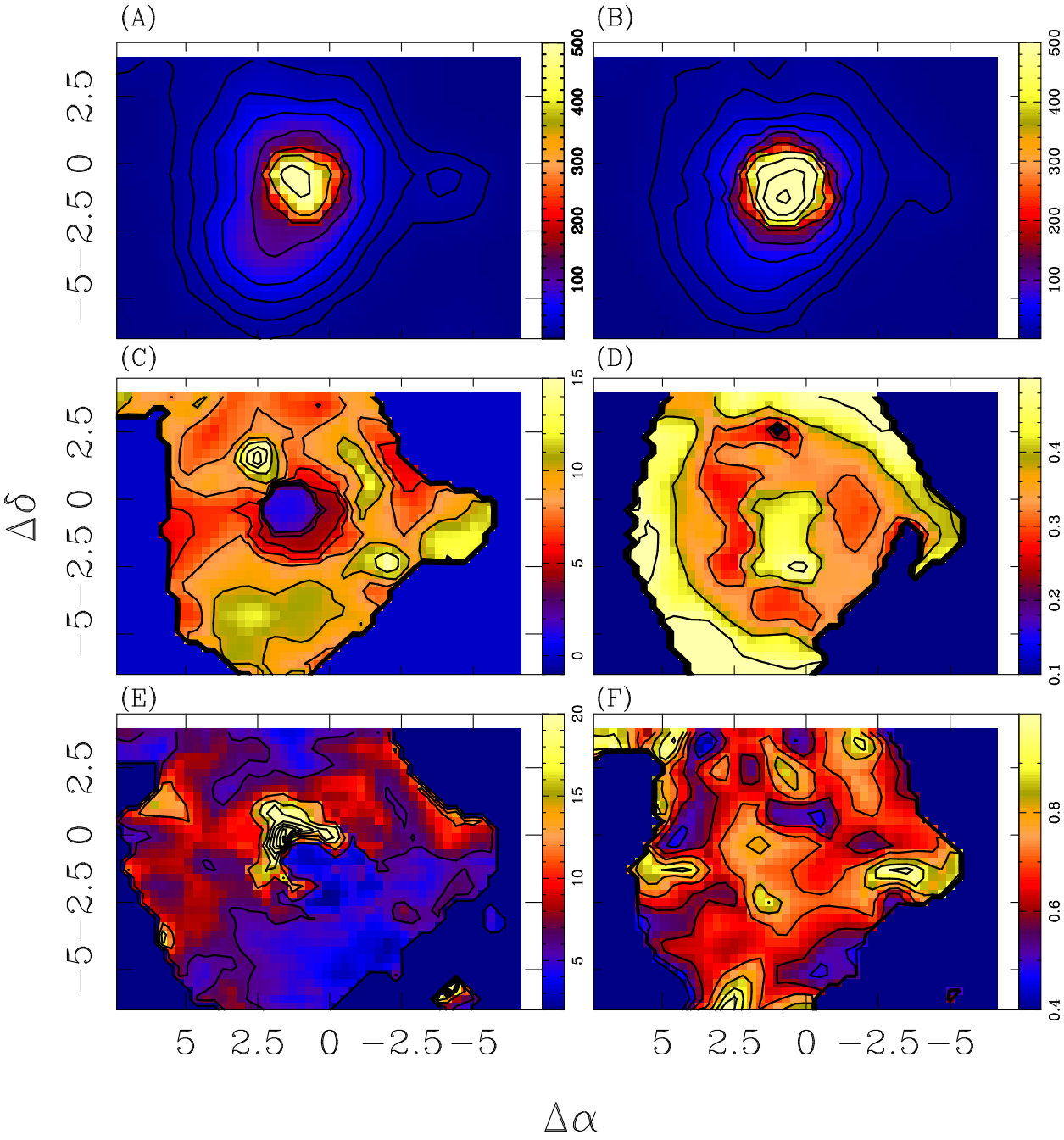

Figure 6: Integrated intensity maps of (A) [OIII]λ5007 and (B) Hα emission lines derived by a Gaussian fitting. In the circumnuclear region, we have included a second broad Gaussian to Hα. Dividing line intensity maps, we have derive: (C) the ionization map [OIII]/H*beta*; (D) [NII]/Hα 2D-distribution; (E) the extinction Hα/Hβ map; and (F) the electronic density distribution [SII]λ6716/[SII]λ6730.

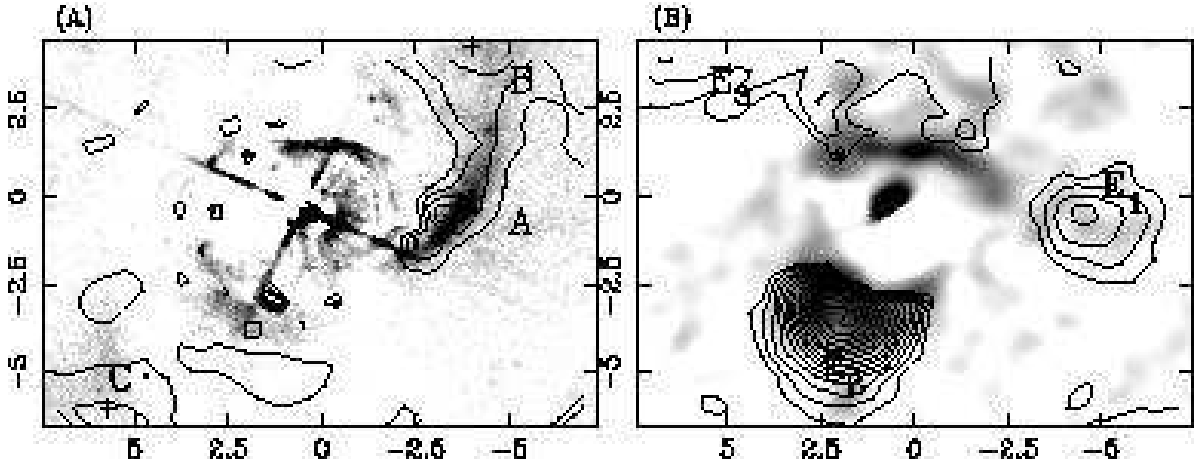

Figure 7: (A) Contour-plot of a narrow-band image centred on the continuum adjacent to the [OIII] emission line (5204-5246Å) extracted from the residual data cube, together with a greyscale of the residual from the 2D modeling of the F555W-band image (Fig. 3D). (B) Contour-plot of a narrow-band image centred on the [OIII]λ5007 emission line (5170-5200Å) extracted from the residual data cube, together with a greyscale of the F555W-F547M image shown in Fig. 3D. The different continuum dominated (left) and emission-line dominated (right) substructures are labelled with their corresponding names.

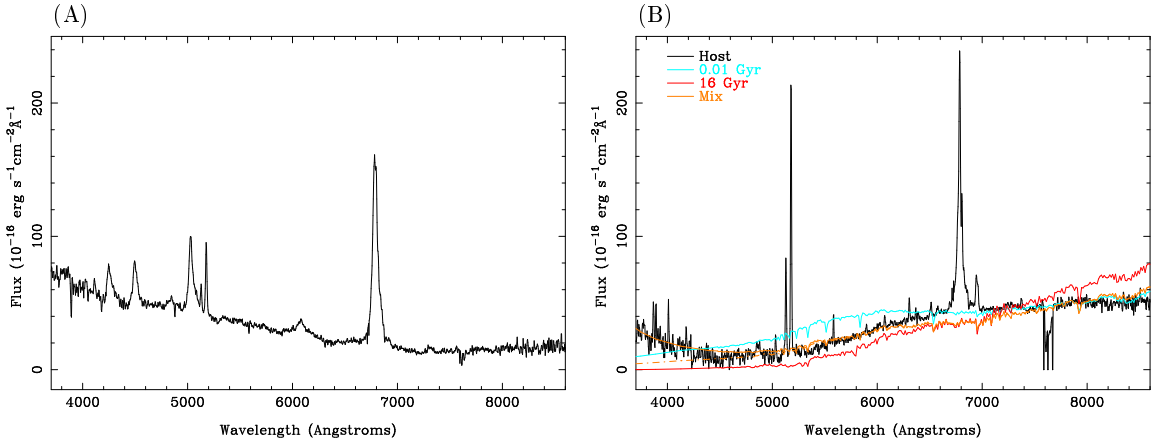

Figure 8: (A) Spectrum of the nucleus of 3C 120, once decontaminated from the contribution of the host galaxy. (B) Spectrum of the host galaxy (black line) together with the spectrum of synthetic models for single stellar populations of 16 Gyr (red line), 0.01 Gyr (blue line), and a mix of both (orange line), adding (solid line) and not adding (dashed line) a power-law continuum to simulate scattered light from the nucleus.

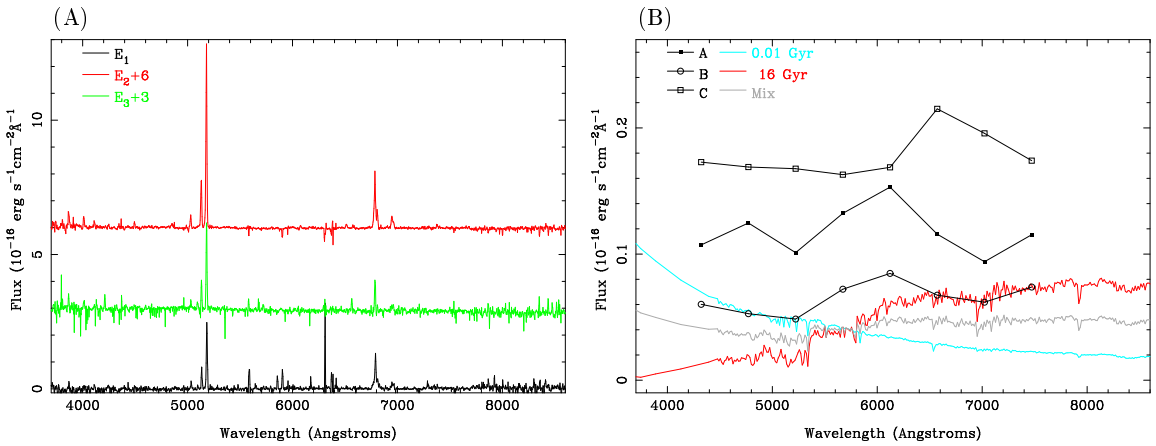

Figure 9: (A) Spectra of the different EELRs detected in the residual data cube. (B) Spectra of the different continuum-dominated structures detected in the residual data cube (points) and a median filtered version of these data (solid lines, solid squares), with a 300Å width.

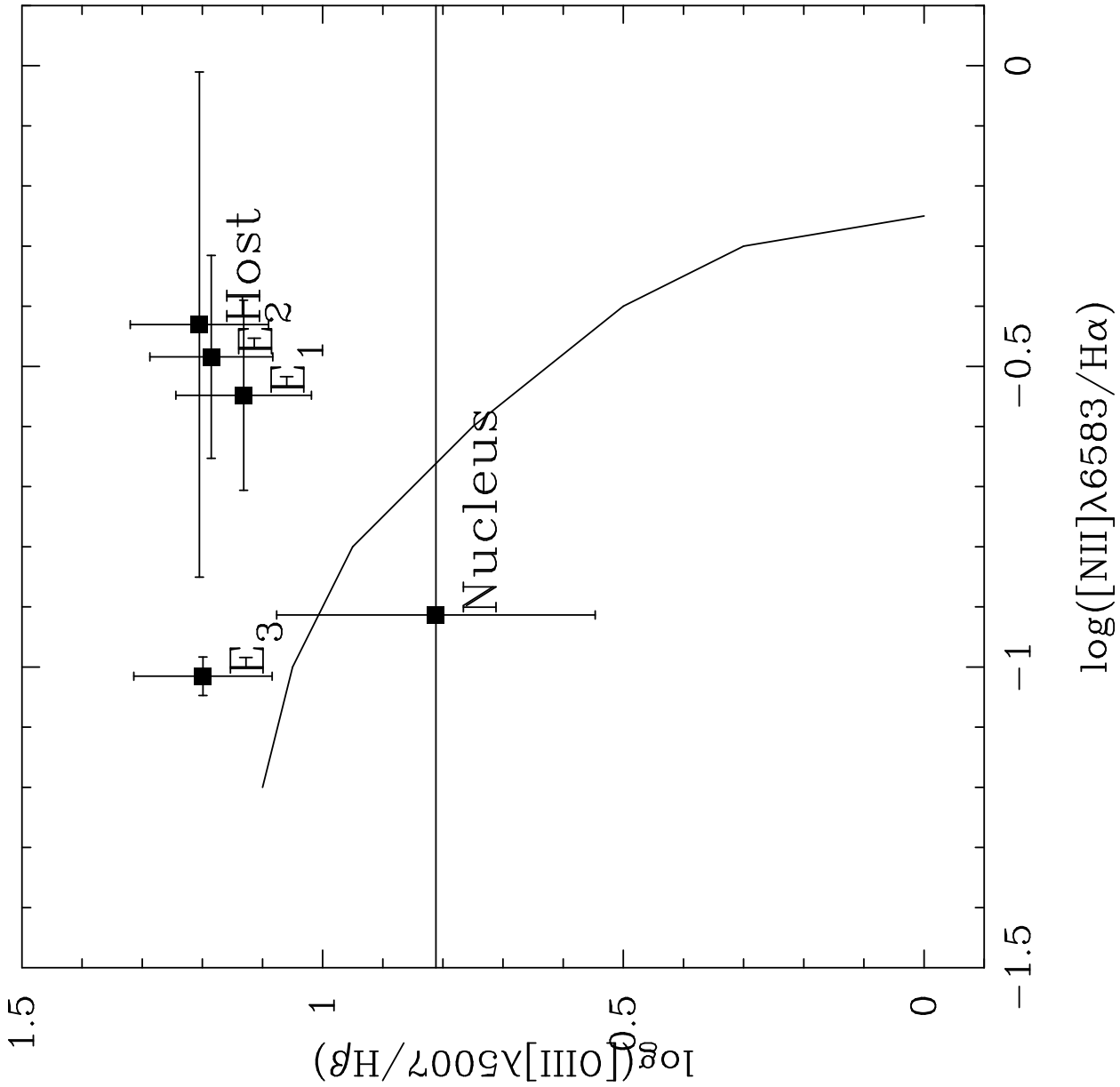

Figure 10: [OIII]λ5007/Hβ vs. [NII]λ6583/Hα intensity ratios for the different components of 3C 120. Solid curve divides AGNs from H_{II} region-like objects.

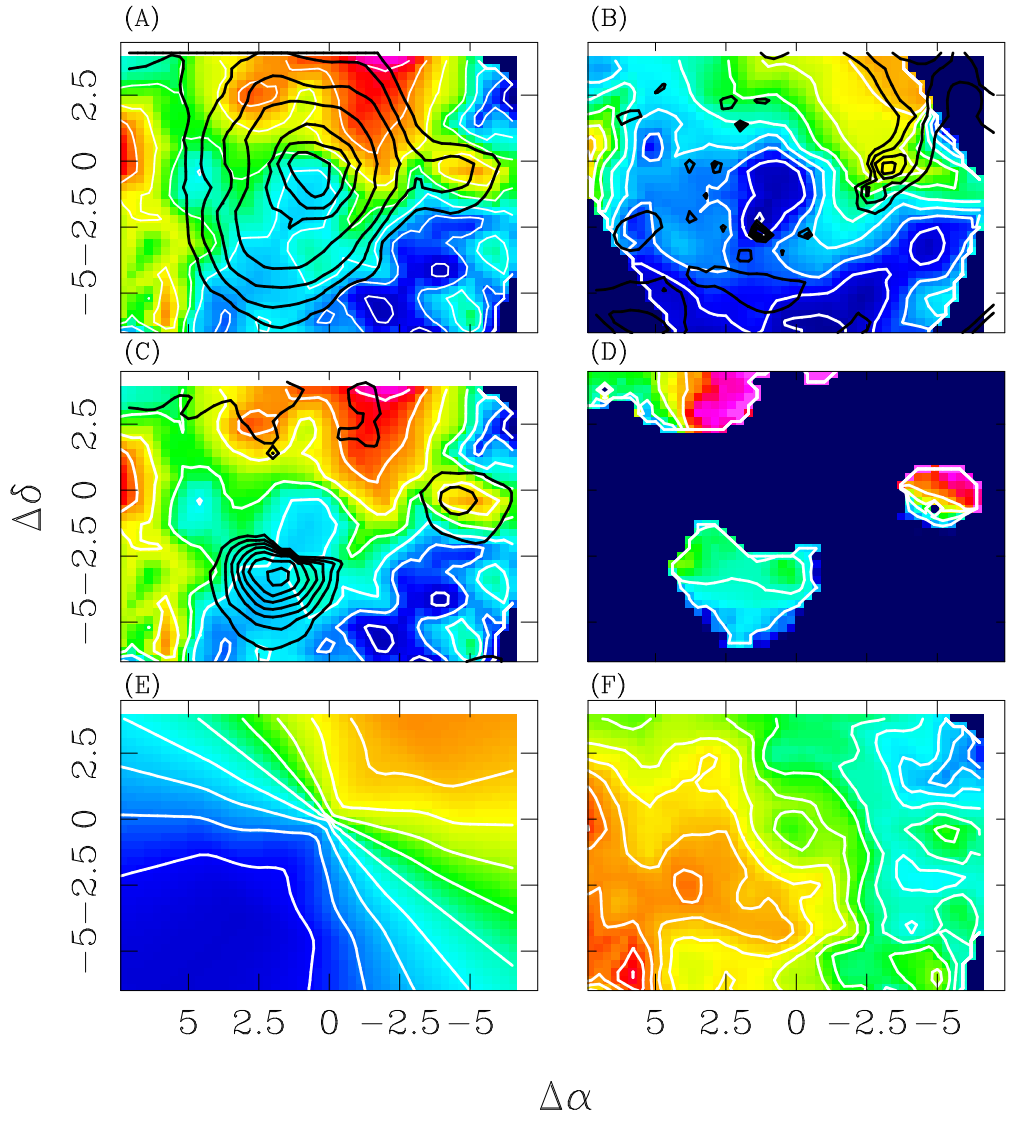

Figure 11: Ionized gas velocity fields of 3C 120 derived from the Gaussian fit to: (A) [OIII], isovelocity lines extend from 10200 to 10600 in steps of 50 km s^{-1}; (B) Hα where isovelocity lines extend from 10000 to 10600 in steps of 50 km s−1. (C) As (A) with the [OIII] intensity of E_1, E_2, E_3 in black contours. (D) The velocity distribution of ionized gas structures (E_1, E_2, E_3). Isovelocity lines extend from 9600 to 10300 in steps of 100 km s^{-1}(E) The simplest rotational model obtained considering an inclination of 40° and PA=-40°. (F) The residual velocity map after the subtraction of the rotational model (E) from the ionized gas velocity field (A). Isovelocity lines corresponds to kinematics of structures E_1, E_2, E_3 as in (D).

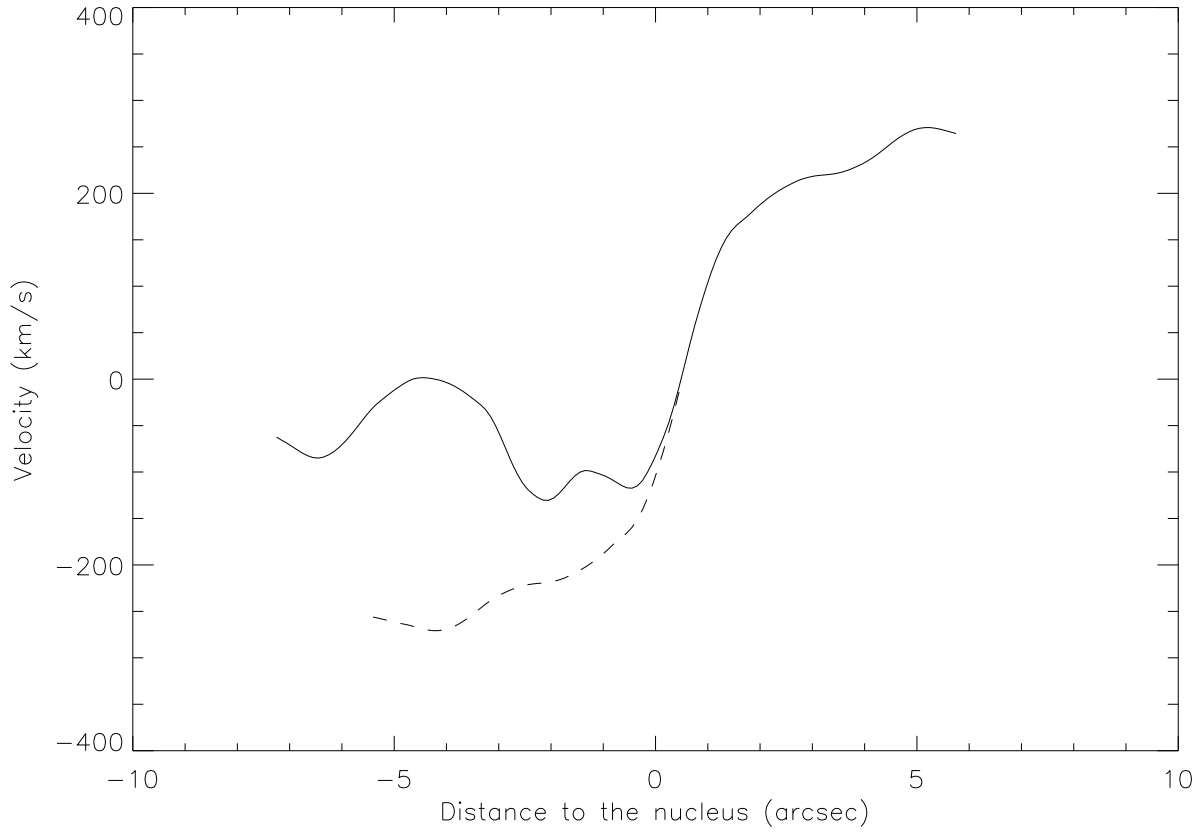

Figure 12: The solid line shows the Hα velocity distribution of 3C 120 along a position angle of $-40°$ from south-east (left) to north-west (right). The perturbation associated with E_2 is seen as a peak at approximately $-5''$. The dashed-line shows the distribution obtained assuming that the north-west portion of the velocity distribution describes the behavior of the rotating component of the galaxy, and modeling the south-east by a symmetrical distribution.

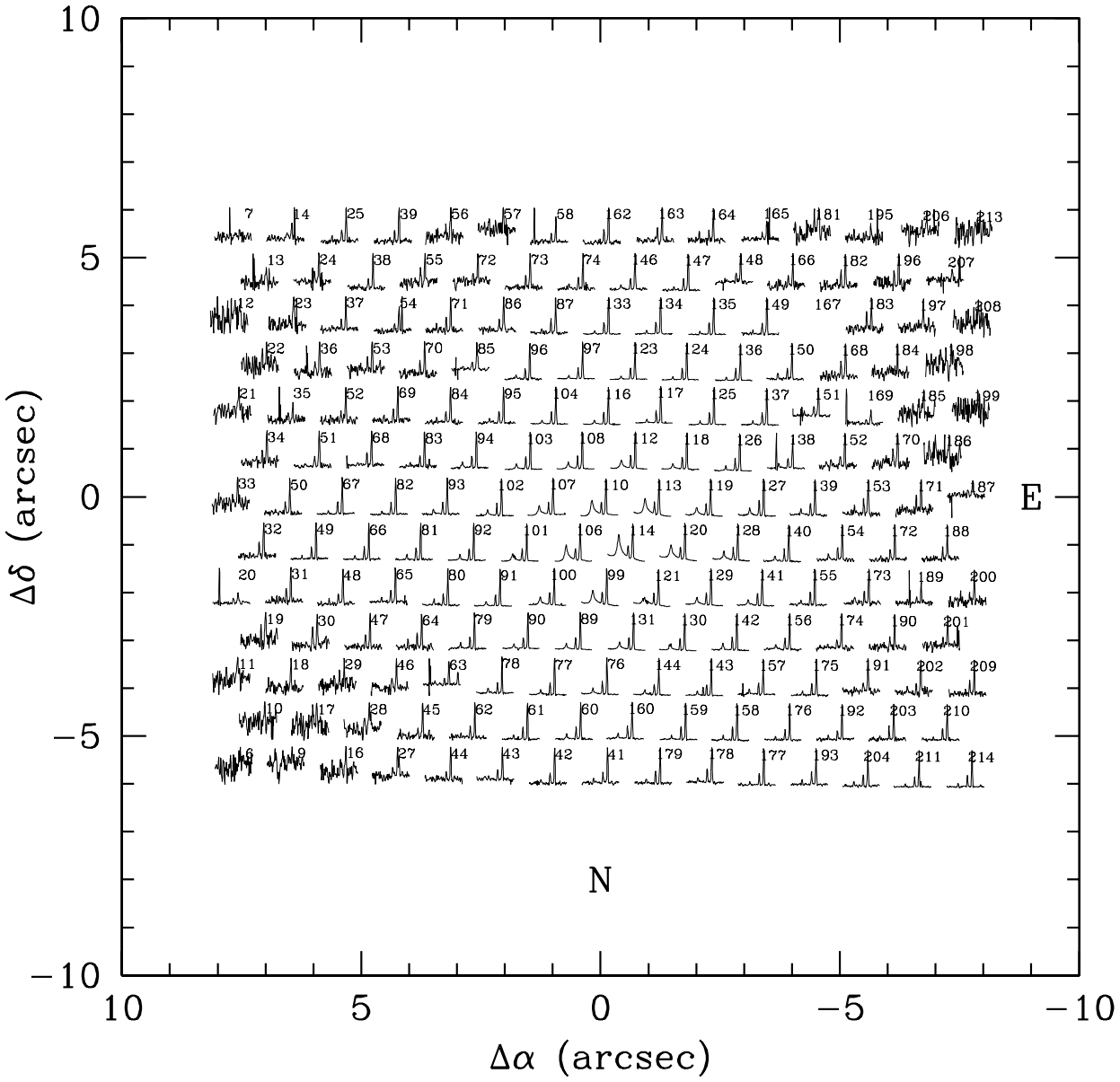

Figure 13: Two-dimensional spectroscopic diagram of Hβ+[OIII]$\lambda\lambda$4959, 5007 emission line profiles. Plotted spectral range: 4910-5300 Å.

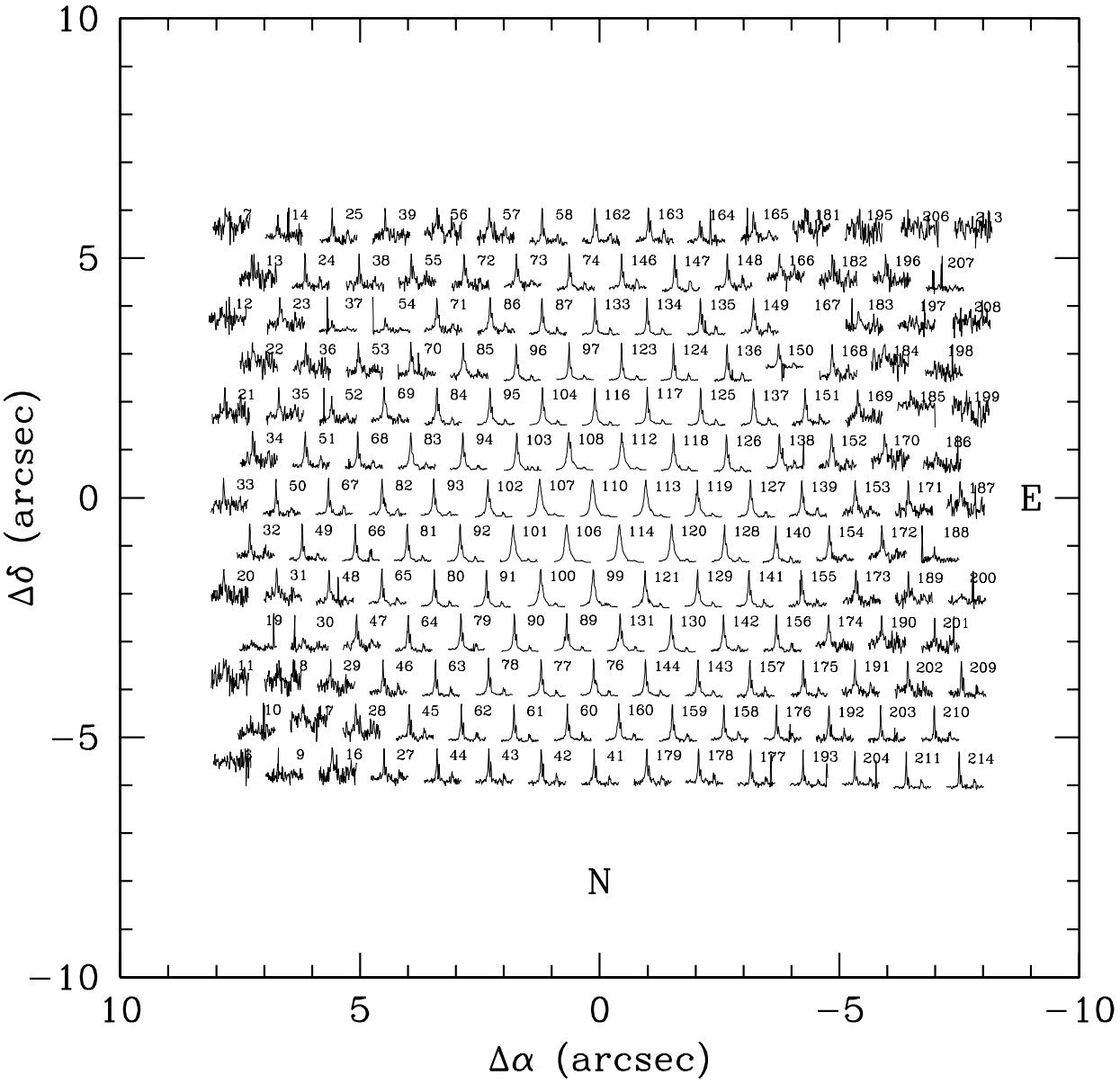

Figure 14: Two-dimensional distribution of emission line profiles of Hα+[NII]$\lambda\lambda$6548, 6584+[SII]$\lambda\lambda$6716, 6730. The spectral range plotted is 6650-7050 Å.

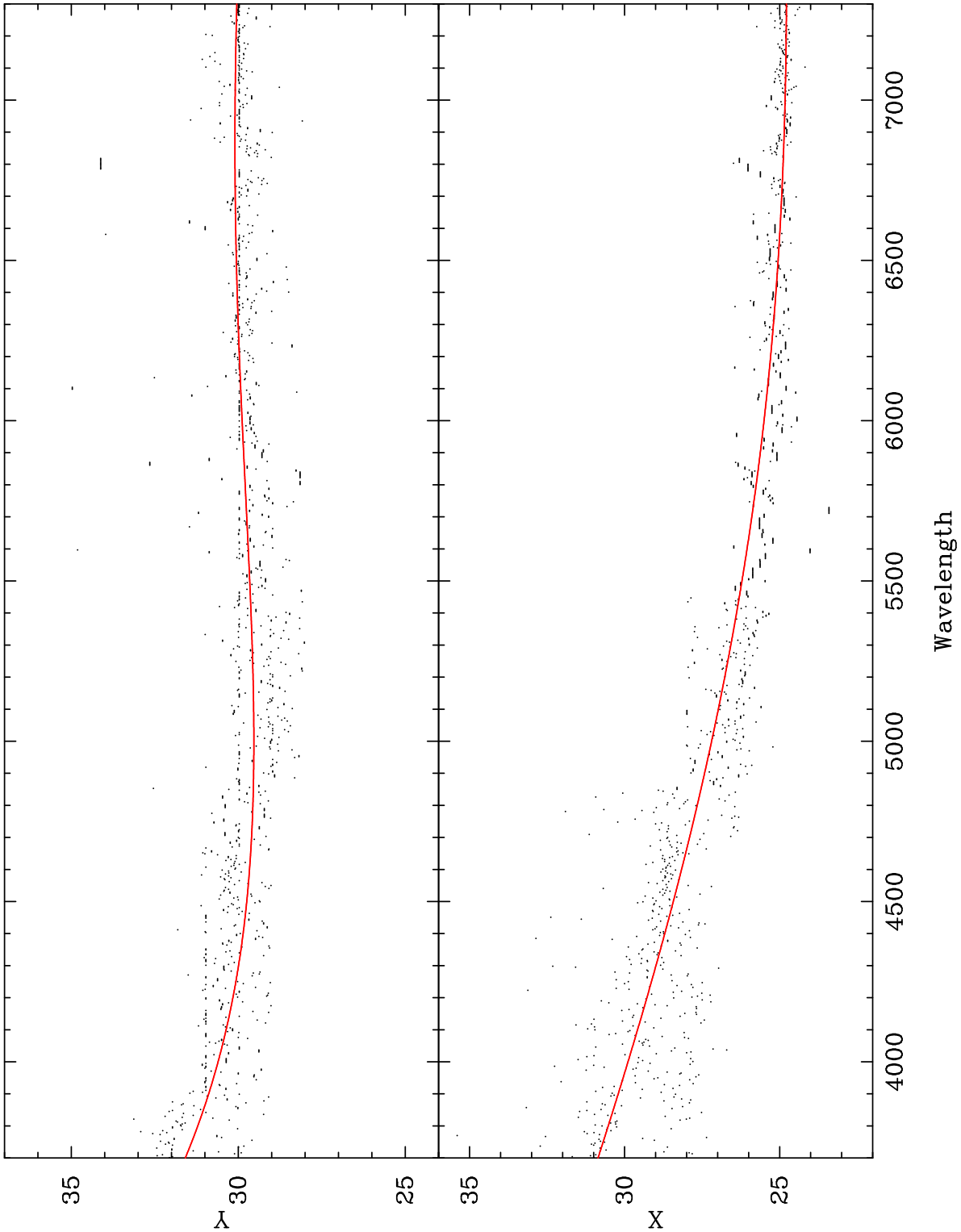

Figure 15: Centroid coordinates, x and y, in pixels ($0\farcs3$/pixel), as a function of the wavelength as derived from the first run of the 3D modeling. The solid-lines show the

result of the fitting with a polynomial function.

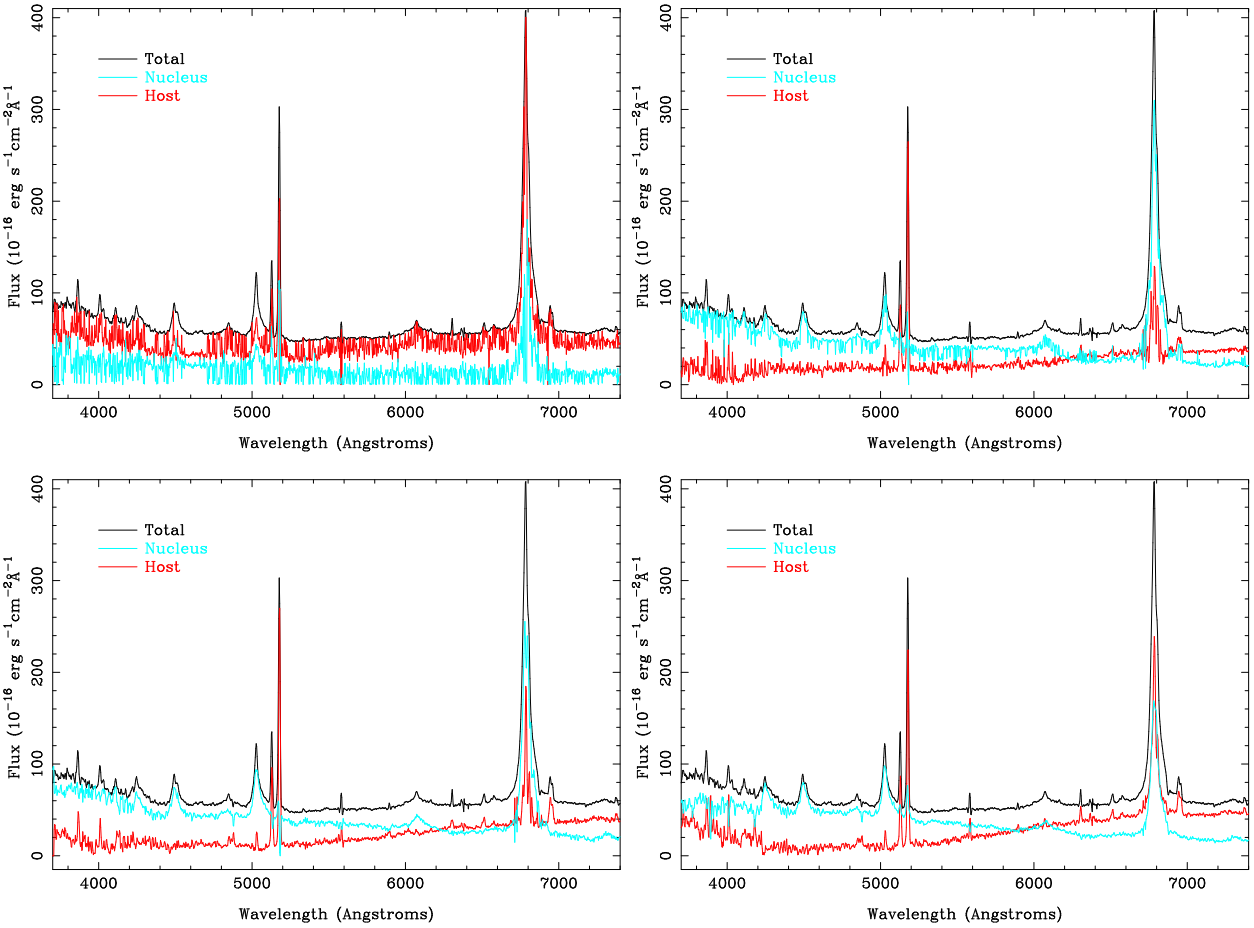

Figure 16: Top-left panel: Decoupled spectra of the nucleus and the host of 3C 120, together with the total spectrum of the object, derived from the 3D modeling when all the parameters are fitted freely. Top-right panel: Similar spectra derived from the modeling when the centroid is fixed to the result of the polynomial function fitting shown in Fig. 15. Bottom-left panel: Similar spectra derived when in addition to the centroids, the ellipticity, position angle and effective radius of the host galaxy are fix to the result of a polynomial function fitting as a function of the wavelength. Bottom-right panel: Final decoupled spectra obtained when the structural parameters of the host galaxy are fixed to the values derived from the 2D modeling of the HST images.

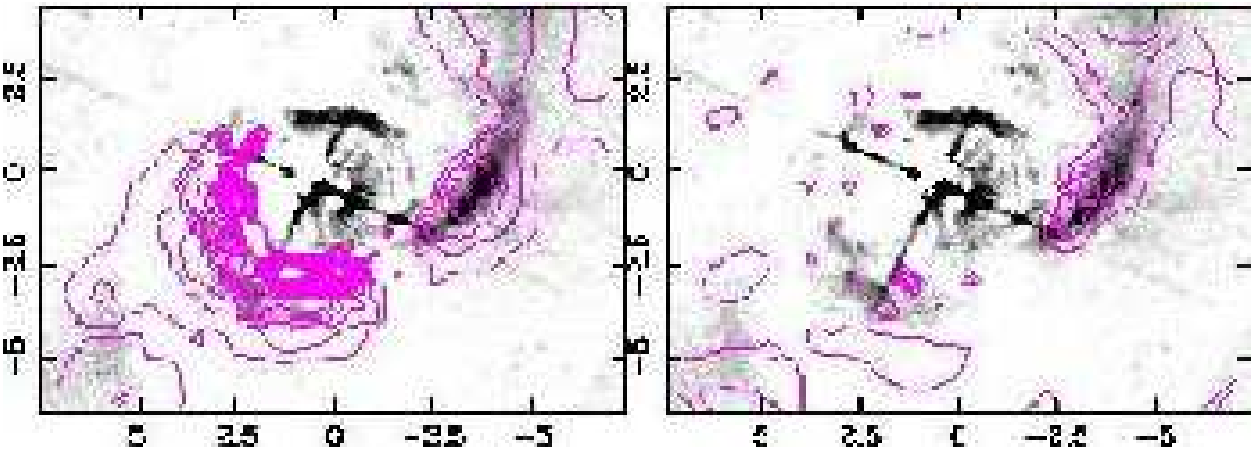

Figure 17: Left panel: Contour-plot of a narrow-band image centred on the continuum adjacent to the [OIII] emission line (5204-5246Å) from the residual datacube obtained by the 3D modeling. Right panel: Contour-plot of a narrow-band image centred on the continuum adjacent to the [OIII] emission line (5204-5246Å) from the residual datacube obtained by the 3D surface brightness analysis. In both panels the grayscale shows the residual from the 2D modeling of the F555W-band image (Fig. 3D)

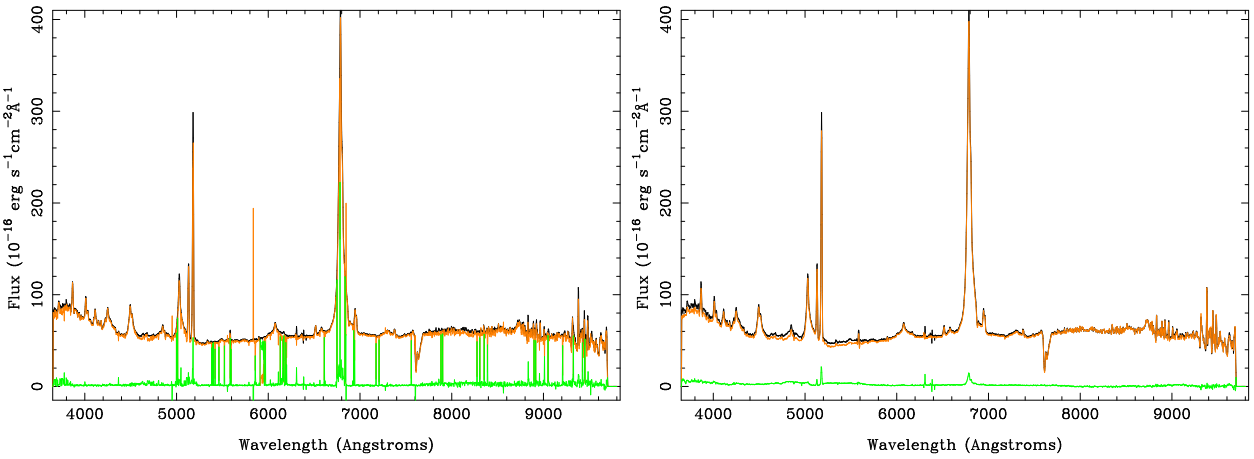

Figure 18: Left panel: Integrated spectrum of 3C 120 (black-line), together with the spectrum of the model (orange) and the residuals (green), obtained using the 3D surface brightness analysis. Right panel: Similar spectra than the ones presented in the left panel obtained once the structural parameters are fixed to the result of a polynomial function fitting as a function of the wavelength.